POLITECNICO DI TORINO

Master's Degree in Energetic and Nuclear Engineering Sustainable Nuclear Energy

Master's Degree Thesis

Development of Improved radioconjugates for Prostate Cancer Theranostics

Centro de Ciencias e Tecnologias Nucleares (IST, Lisbon)

Supervisors:
Prof. Diana Massai
Prof. Célia Maria da Cruz Fernandes (C2TN/IST)
Prof. Filipa Fernandes Mendes (C2TN/IST)

Candidate:
Giorgia Carnà

November 2025

'Life is a climb but the view is great'.

Abstract

Prostate cancer is one of the most common malignancies in men, and the prostate-specific membrane antigen (PSMA) has emerged as a key molecular target for imaging and targeted radionuclide therapy (TRT). However, current PSMA-targeted radiopharmaceuticals often display rapid blood clearance and high renal uptake, which can limit their therapeutic performance.

This work focused on the design, synthesis, and preclinical evaluation of a novel heterobivalent radiocomplex aimed at improving the pharmacokinetic properties of PSMA-targeted agents. The developed conjugate, IPBA–PEG–DOTA–PSMA, integrates a PSMA-binding moiety with an albumin-binding unit, 4-(p-iodophenyl)butyric acid (IPBA), to promote a reversible interaction with serum albumin. This dual-targeting strategy was intended to prolong systemic circulation and enhance tumor accumulation while minimizing non-specific uptake.

The conjugate was synthesized through a stepwise procedure enabling the independent coupling of the PSMA-recognition and albumin-binding fragments. Radiolabeling with Indium-111 was achieved in high yield, affording [^{111}In]In–IPBA–PEG–DOTA–PSMA with excellent radiochemical purity and stability in both PBS and serum. Indium-111 was employed as the γ-emitting isotope for imaging and biodistribution studies, while the same DOTA chelator allows for complexation with Lutetium-177, supporting a theranostic application.

In vitro assays performed on PSMA-positive (PC3-PIP) and PSMA-negative (PC3-FLU) prostate cancer cell lines confirmed a receptor-mediated uptake mechanism. Serum-binding studies demonstrated the expected interaction with albumin. Biodistribution experiments in healthy CD-1 mice revealed prolonged blood retention and slower clearance for the heterobivalent compound compared to the PSMA-only reference complex.

Overall, the incorporation of the IPBA-based albumin-binding domain effectively improved the pharmacokinetic and biological profile of PSMA-targeted radiocomplexes, supporting its potential as a promising theranostic agent for prostate cancer.

Sommario

Il carcinoma prostatico è una delle neoplasie più comuni negli uomini e rappresenta una delle principali cause di mortalità per cancro a livello mondiale. L'antigene di membrana specifico della prostata (PSMA) è emerso come un importante bersaglio molecolare per l'imaging e per la terapia radionuclidica mirata (TRT). Tuttavia, i radiofarmaci diretti al PSMA attualmente disponibili mostrano spesso una rapida eliminazione dal sangue e un'elevata captazione renale, fattori che possono ridurne l'efficacia terapeutica.
Questo lavoro è stato focalizzato sulla progettazione, sintesi e valutazione preclinica di un nuovo radiocomplesso eterobivalente, sviluppato con l'obiettivo di migliorare le proprietà farmacocinetiche dei composti diretti al PSMA. Il coniugato sviluppato, IPBA–PEG–DOTA–PSMA, integra una porzione legante il PSMA con un'unità legante l'albumina, rappresentata dall'acido 4-(p-iodofenil)butirrico (IPBA), progettata per favorire un'interazione reversibile con l'albumina sierica. Questa strategia di duplice targeting è stata concepita per prolungare la circolazione sistemica e aumentare l'accumulo tumorale, riducendo al contempo la captazione non specifica.
Il coniugato è stato sintetizzato tramite una procedura graduale che ha permesso il legame indipendente delle unità di riconoscimento del PSMA e di legame all'albumina. La marcatura radioattiva con l'Indio-111 è stata ottenuta con alta resa, fornendo [^{111}In]In–IPBA–PEG–DOTA–PSMA eccellente purezza radiocomica e stabilità sia in PBS che in siero. L'Indio-111 è stato impiegato come isotopo γ-emittitore per studi di imaging e biodistribuzione, mentre lo stesso chelante DOTA consente la complessazione con Lutezio-177, permettendo un'applicazione di tipo teranostico.
I saggi *in vitro* condotti su linee cellulari di carcinoma prostatico PSMA-positive (PC3-PIP) e PSMA-negative (PC3-FLU) hanno confermato un meccanismo di captazione mediato dal recettore. Gli studi di legame sierico hanno mostrato l'interazione attesa con l'albumina mentre gli esperimenti di biodistribuzione eseguiti su topi sani CD-1 hanno evidenziato una più lunga permanenza nel sangue e una più lenta eliminazione per il composto eterobivalente rispetto al complesso di riferimento diretto solo al PSMA.
Nel complesso, l'introduzione del dominio legante l'albumina basato su IPBA ha migliorato in modo significativo il profilo farmacocinetico e biologico dei radiocomplessi diretti al PSMA, confermando il potenziale di questo nuovo coniugato come promettente agente teranostico per il carcinoma prostatico.

Aknowledgments

Thank to my supervisors from Tecnico of Lisbon, Dr. Filipa Mendes and Dr. Celia Fernandez, for welcoming me and giving me the opportunity to take part in this experience.
In particular, I would like to thank Celia for all the hours spent together in the chemistry laboratory, patiently teaching me such a complex subject in just a few months and explaining every concepts to me as many times as I needed.
This experience truly pushed me out of my comfort zone and allowed me to challenge myself, so I am deeply grateful to have had both of you as my mentors and support throughout this journey.

Grazie alla mia famiglia: mamma, papà e mia sorella Sara per avermi accompagnato in questo lungo viaggio sostenendomi in ogni mia scelta, senza mai permettermi di buttarmi giù di fronte alla avversità.

Grazie, inoltre a Leonardo e a tutti i miei amici perché mi avete sempre regalato momenti di svago e alleggerito tutte queste intense giornate trascorse insieme.

Contents

List of Figure

List of Table

Chapter 1

Introduction

1.1 Overview of the prostate cancer

Prostate cancer represents a major health issue in men. It is frequently diagnosed in association with secondary malignancies and ranks as the sixth leading cause of cancer-related mortality among men worldwide [1]. Prostate cancer is the second most common cancer in men after lung cancer, accounting for about 7% of all new cancer cases in males worldwide and up to 15% in developed countries. Every year, over 1.2 million new cases are diagnosed, and more than 350,000 men die from the disease, making it one of the main causes of cancer-related death in men [2]. It is largely regarded as a disease of old age, with a peak incidence observed in men around 70 years of age [3]. The prostate is a gland of the male reproductive system, located below the bladder and surrounding the urethra. Its main function is the production of seminal fluid components, which are essential for ejaculation and sperm viability. In the adult prostate, three main zones can be identified: central, transition and peripheral, along with fibromuscular and periurethral regions. Structurally, the gland is composed of ducts and acini embedded in stromal tissue, lined by luminal and basal epithelial cells as illustrated in figure 1.1. Luminal cells have a secretory role and express high levels of the androgen receptor, while basal cells express specific markers but only low levels of the receptor; rare neuroendocrine cells are also present [2], [4].

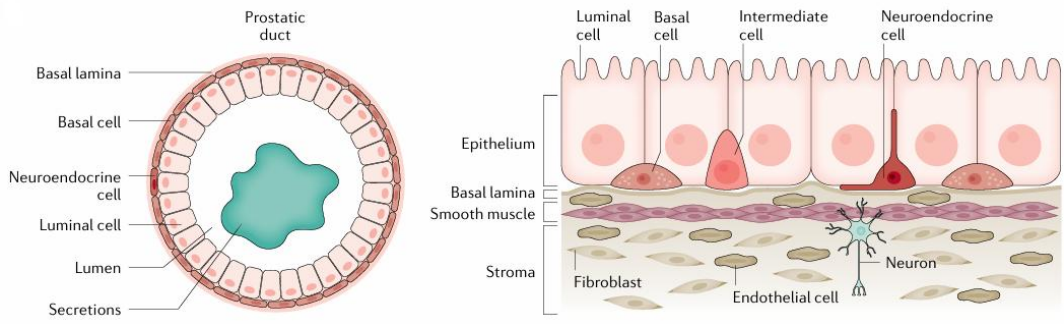

Figure 1.1: Histological structure of the human prostate gland. Adapted from [2].

The development of prostate cancer is a gradual process. In many cases, it begins early in life in a localized and silent form, known as prostatic intraepithelial neoplasia (PIN). PIN is an asymptomatic but histologically detectable lesion, characterized by an abnormal growth of luminal cells and the progressive loss of basal and secretory cell layers. High-grade PIN is regarded as a direct precursor of adenocarcinoma, although not every lesion inevitably progresses to invasive disease. With time, the accumulation of genetic alterations can drive PIN to evolve into a localized prostate tumor capable of metastasizing as shown in figure 1.2. Once adenocarcinoma develops, two main phases are recognized [4], [5]:

- the androgen-dependent stage, which may remain latent or become clinically evident and is marked by the complete loss of basal cells and a pronounced luminal phenotype
- the androgen-independent or castration-resistant stage, which represents the advanced phase of the disease. At this point, tumor growth is no longer sustained by androgens and the disease becomes more aggressive and tends to spread [4], [5].

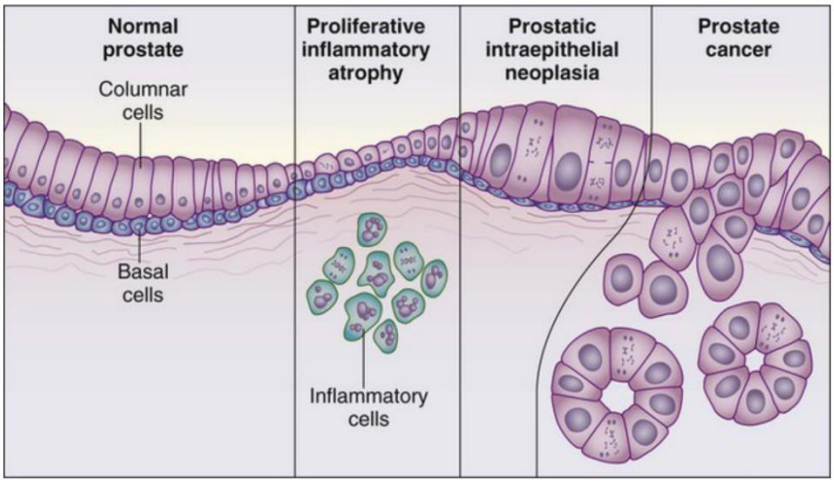

Figure 1.2: Proliferative inflammatory atrophy (PIA) as a precursor to prostatic intraepithelial neoplasia (PIN) and prostate cancer. Adapted from [6].

In patients with localized prostate cancer, the main treatment options are radical prostatectomy or radiotherapy, given either as external beam radiation or brachytherapy and these are still the most common approaches in primary treatment [7].
However, prostate cancer growth is strongly influenced by androgens hormones made in the testes, adrenal glands, and the prostate itself, which are important for normal prostate function but also stimulate tumor proliferation. For this reason, therapies that block androgen activity are widely used, with androgen deprivation therapy (ADT) representing the standard approach to delay or prevent disease progression. Nevertheless, the benefit of ADT is temporary, as most patients eventually progress to castration-resistant prostate cancer (CRPC). In addition, castration is linked to several adverse effects, including loss of libido, reduced muscle and bone mass and a higher risk of metabolic syndrome, cardiovascular disease, and mortality [8].
As disease progression leads to considerable mortality and morbidity, the development of new and targeted treatments is urgently required. Prostate cancer represents an excellent target for the development of targeted therapies for several reasons:

- the prostate is a non vital organ, which allows the use of treatments directed against tissue-specific antigens with limited risk to essential organs
- prostate cancer metastases are most often found in lymph nodes and bones, sites that are well supplied with circulating antibodies, facilitating drug delivery
- metastases are usually small in size, which improves antibody access and penetration

- the prostate-specific antigen (PSA) serum marker provides a means for the early detection of metastases and the monitoring of therapeutic efficacy [7].

1.2 Radioactivity

Radioactivity is the process by which an unstable nucleus changes into one or more daughter nuclei that are more stable. This transformation does not always happen in a single step: sometimes the daughter nucleus is still unstable and continues to decay through a chain of transformations until a stable state is reached [9].
Each decay is usually accompanied by the release of energetic particles that may be used in science, industry, agriculture, and medicine [9], [10]. A radiation is ionizing when it has enough energy to remove electrons from atoms or molecules, creating ions in the material it passes through.
In order to do this, the radiation must carry sufficient energy to break the bond between an electron and its atom. In practice, energies of just a few tens of electronvolts (1 eV = 1.6×10^{-19} J) are enough to cause ionization [11]. Figure 1.3 illustrates the distinction between non-ionizing and ionizing radiation across the electromagnetic spectrum.

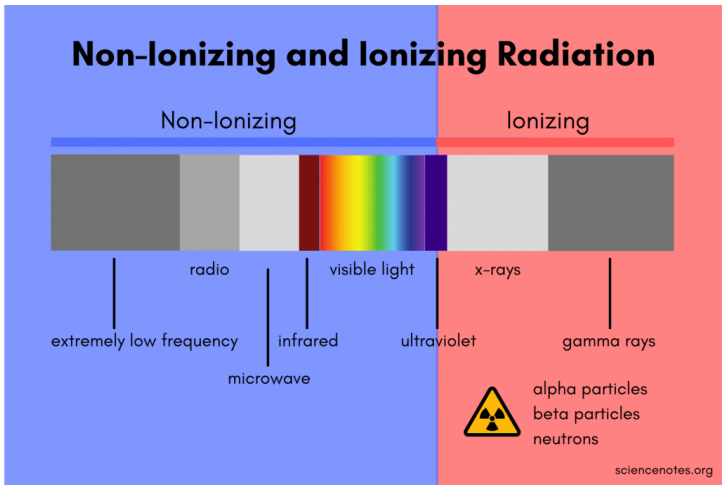

Figure 1.3: Non-ionizing and ionizing radiation. Adapted from [12].

1.2.1 Radioactive decay law

Radioactive decay describes the transformation of an unstable parent nucleus (P) into a more stable daughter nucleus (D):

$$P \xrightarrow{\lambda_p} D \tag{1.1}$$

This process is governed by the decay constant λ, which is a fundamental property of each radionuclide. The decay constant is independent of the age of the atom and essentially unaffected by external conditions such as temperature, pressure, or chemical state. It has the dimension of reciprocal time, usually expressed in s^{-1} [9].
The rate of decrease of the number of parent nuclei N(t) is proportional to the number of nuclei present at time t [9], [13]:

$$\frac{dN_p(t)}{dt} = -\lambda_p N_p(t) \tag{1.2}$$

Above, the fundamental differential equation of radioactive decay can be rearranged into integral form as [9]:

$$\int_{N_p(0)}^{N_p(t)} \frac{dN_p(t)}{N_p(0)} = -\int_0^t \lambda_p dt \tag{1.3}$$

where $N_p(0)$ is the number of radioactive nuclei at time t = 0 [9].
Assuming λ_p constant, integral (1.3) can be solved as follow [9]:

$$ln\frac{N_p(t)}{N_p(0)} = -\lambda_p t \tag{1.4}$$

resulting in the exponential decay law [9], [13]:

$$N_p(t) = N_p(0)e^{-\lambda_p t} \tag{1.5}$$

Equation 1.5 shows that radioactive nuclei decreases according to an exponential law (figure 1.4), with the rate of decay determined by the decay constant.

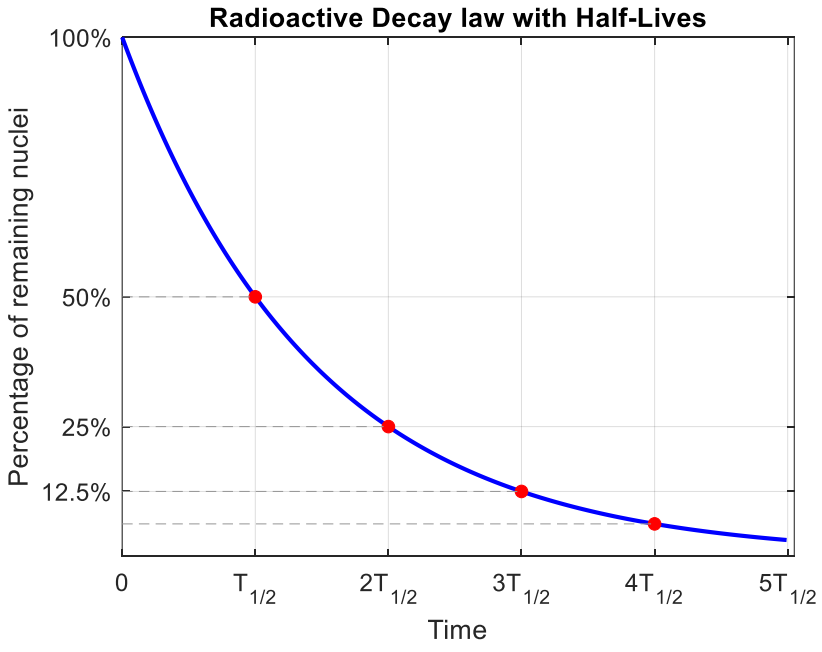

Figure 1.4: Radioactive decay law.

The activity A(t) defined as the total number of disintegrations per unit time, is the product of the decay constant and the number of radioactive nuclei [9]:

$$A(t) = \lambda_p N_p(t) \qquad (1.6)$$

The SI unit of activity is the becquerel (Bq), equal to one decay per second (1 Bq = 1 $\frac{\text{decay}}{\text{s}}$). The becquerel (Bq) and the Curie (Ci) are related as: $1\ \text{Bq} = 2.703 \times 10^{-11}\text{Ci}$ or $1\ \text{Ci} = 3.7 \times 10^{10}\ \text{Bq}$ [9].

Half life

Half-life ($t_{1/2}$) is the time it takes for half of the unstable nuclei, in a sample, to decay [14]:

$$N_p\big((t_{1/2})_p\big) = \frac{1}{2}N_p(0) = N_p(0)e^{-\lambda(t_{1/2})_p} \qquad (1.7)$$

From (1.7) the following relations is obtained [9] :

$$\lambda_p = \frac{ln\,(2)}{(t_{1/2})_p} \qquad (1.8)$$

Mean life

The mean life of a radioactive substance P is the total lifetime of all its atoms divided by the number of radioactive nuclei present at the beginning, it represents the inverse of the decay constant [9]:

$$\tau_\text{p} = \frac{1}{\lambda_\text{p}} \qquad (1.9)$$

The meal life is linked to the half life through the following expression [9]:

$$\tau_p = \frac{1}{\lambda_p} = \frac{(t_{1/2})_p}{ln\,(2)} \approx 1.44(t_{1/2})_p \qquad (1.10)$$

1.2.2 Types of radioactive decay

An unstable nucleus ${}^{A}_{Z}X$ characterized by an atomic number (Z) and mass number (A), can undergo 4 main different types of spontaneous radioactive decay to reach more stable configurations as shown in figure (1.5):

- Alpha decay (α)
- Beta decay (β)
- Gamma decay (γ)
- Electron capture

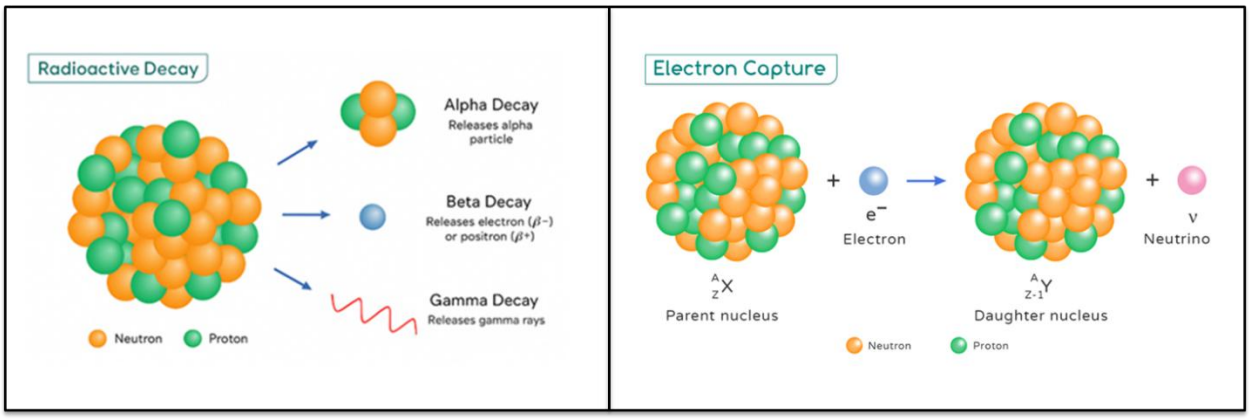

Figure 1.5: Main types of radioactive decay, including alpha, beta, and gamma emission (left), and electron capture (right). Adapted from [14].

α decay

It is a nuclear transformation in which an unstable parent nucleus P becomes more stable by emitting an α particle. The α particle, corresponding to a helium-4 nucleus, is particularly stable thanks to its binding energy of about 7 MeV per nucleon. In this decay, a ${}^{4}_{2}$He nucleus is emitted, in this way the parent reduces the nucleus by 2 protons and 2 neutrons, so that its mass number A decreases by 4 and its atomic number Z by 2 [9].

$$ {}^{A}_{Z}P \rightarrow {}^{A-4}_{Z-2}D + {}^{4}_{2}He \qquad (1.11) $$

Since the nucleus loses two protons, the atom also releases two orbital electrons to preserve electrical neutrality.

β decay

In this type of radioactive decay, a nucleon inside the nucleus undergoes a transformation that changes its identity. In neutron-rich nuclei, a neutron is converted into a proton with the emission of an electron and an antineutrino (β^- decay). Conversely, in proton-rich nuclei, a proton is converted into a neutron with the emission of a positron and a neutrino (β^+ decay). As a result, Z of the parent nucleus changes by ±1, while A remains the same [9], [15].

- $\boldsymbol{\beta^-}$

$$ {}^{A}_{Z}P \rightarrow {}^{A}_{(Z+1)}\{D\} + e^- + \bar{\nu}_e \qquad (1.12) $$
$$ n \rightarrow p + e^- + \bar{\nu}_e $$

- β^+

$$ {}^{A}_{Z}P \rightarrow {}_{(Z-1)}{}^{A}\{D\} + e^+ + \nu_e \qquad (1.13) $$
$$ p \rightarrow n + e^+ + \nu_e $$

γ decay

A nucleus in an excited state can decay to its ground state, or to a lower energy state, by emitting electromagnetic radiation:

$$ {}^{A}_{Z}P^* \rightarrow {}^{A}_{Z}P + \gamma \qquad (1.14) $$

This process occurs when the excitation energy is too low to cause the emission of a nucleon. Excited nuclei can be produced through nuclear reactions, γ-ray absorption, or as a result of α or β decay, where the daughter nucleus is often left in an excited state. The nucleus then releases one or more γ photons until it reaches its ground state [9], [15].

Electron capture

It is a type of radioactive decay in which an atomic nucleus absorbs an inner atomic electron. This process leads to the transformation of a proton into a neutron and a neutrino. The neutrino is emitted from the nucleus, conserving energy and momentum., resulting in a change of the element. This process is significant in elements with a large number of protons, where the strong nuclear force is counterbalanced by electrostatic repulsion among protons [16].

$$ {}^{A}_{Z}P + e^- \rightarrow {}_{Z-1}{}^{A}D + \nu_e \qquad (1.15) $$

As a result, A remains unchanged, Z decreases of 1, leaving the atom in an excited state with a primary orbital vacancy [16], [17].

1.2.3 Biological effects of ionizing radiation

The four types of decay described above are all considered ionizing radiations, as they have enough energy to remove electrons from atoms and molecules. Some types of radioactive decay release ionizing particles directly. In α decay, the nucleus emits an α particle, while in β decay it emits an electron (β^-) or a positron (β^+). These particles are directly ionizing, depositing energy along their tracks as they move through tissue.

In contrast, γ-rays and X-rays are photons with no charge; their biological effects arise mainly from interactions with matter, such as the photoelectric effect and Compton scattering, which eject secondary electrons [18], [19].

Ionizing radiation, whether in the form of photons or particles like α and β, transfers energy to cells by ejecting electrons from atoms and molecules. This process causes ionization leading to chemical bond disruption, and creations of free radicals [18]. As these particles and secondary electrons travel through the cell, they create additional ionizations along their paths. Toward the end of their tracks, interactions become more concentrated, forming clusters of ionizations [19].

DNA is the most important target of radiation. With high-LET particles, most of the damage results from direct interactions with the DNA itself. Indirect effects occur instead when radiation interacts with other cellular molecules, generating reactive oxygen species (ROS) such as free radicals (•OH, •H), as well as O_2 and H_2O_2, produced from the radiolysis of water [20], [21].
These reactive products can break chemical bonds and induce chemical modifications that ultimately lead to DNA damage [21]. Figure 1.6 shows that when such clusters occur near DNA, multiple lesions may appear within just a few base pairs including base modifications, single-strand breaks (SSBs) and double-strand breaks (DSBs) [18], [19]. The extent of biological damage depends strongly on the linear energy transfer (LET), which describes the energy deposited per unit path length (keV/µm). Table 1.1 summarizes the typical energy, range, and LET values for α and β particles, illustrating their different ionization properties. High-LET radiations, such as α-particles, produce dense ionization tracks and complex DNA lesions but penetrate only a few cell diameters. Low-LET radiations, such as γ-rays, penetrate deeply but generate sparse ionizations, while β particles have intermediate properties. Because of this, the relative biological effectiveness (RBE) of high-LET radiation is usually higher than that of low-LET radiation: for the same absorbed dose, α particles are generally more effective at killing cells than γ or β radiation [18], [22].

Table 1.1: Characteristic of alpha and beta particles. Adapted from [22].

Decay	$E_{min} - E_{max}$	Range in tissue	LET
α particle	5 to 9 MeV	40 to 100 µm	~80 keV/µm
β particle	50 to 2300 keV	0.05 to 12 mm	~0.2 keV/µm

When DNA lesions cannot be repaired, cells may die through different mechanisms. The most common are: apoptosis (programmed cell death), necrosis (uncontrolled breakdown), mitotic catastrophe (failure during cell division) and senescence (permanent growth arrest) [18].

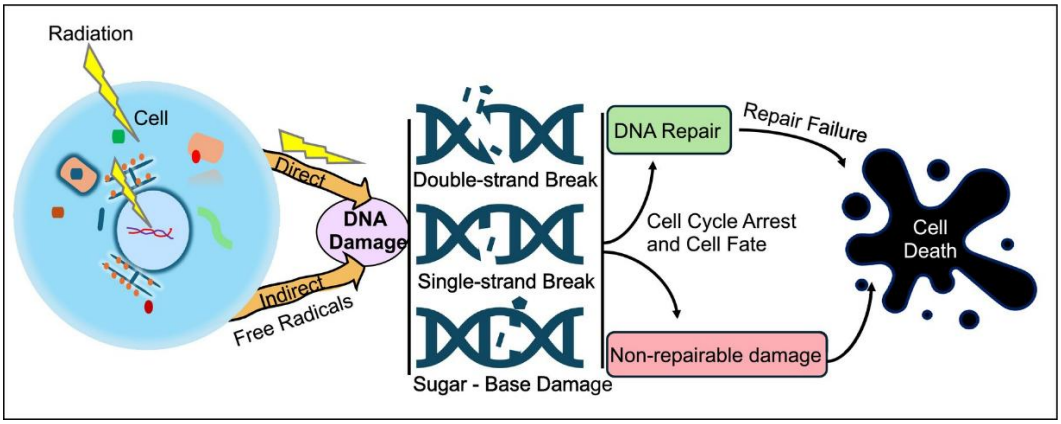

Figure 1.6: Ionizing radiation induced DNA damage and cell death. Adapted from [23].

1.3 Radiation therapy

Although radiation affects both healthy and cancerous cells, the aim of radiation therapy is to deliver the highest possible dose to the tumor while limiting exposure to nearby normal tissues. Healthy cells are usually able to repair radiation-induced damage more efficiently and return to normal function, thanks to active DNA repair enzymes that maintain genomic stability. In contrast, cancer cells often have defective repair pathways due to mutations in these enzymes, making them more likely to die after treatment [24]. Based on these principles, radiation therapy can be delivered either externally, through external beam radiotherapy (EBRT), or internally, through brachytherapy.

1.3.1 External beam radiotherapy

Figure 1.7 illustrates EBRT, in which radiation is delivered from a machine that directs beams precisely at the tumor. It is considered a local treatment, since the radiation targets only a specific part of the body [25].

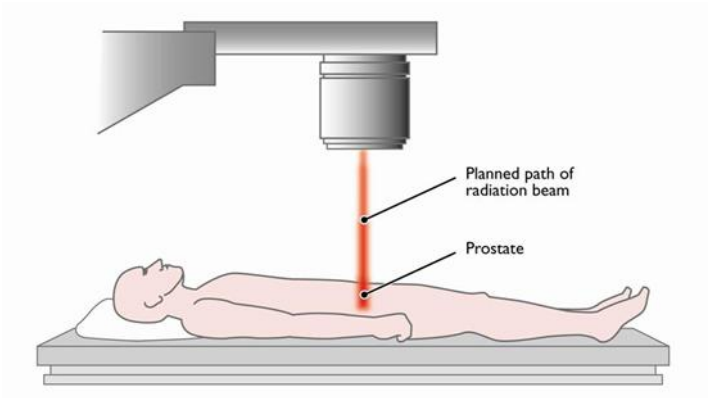

Figure 1.7: Schematic representation of EBRT for prostate cancer. Adapted from [25].

The radiation can be delivered through three types of beams:

- **Photons**: Most EBRT machines use high energy photon beams. Photon beams can penetrate deep into the body, making them suitable for tumors located in internal organs. However, as photons travel through tissue, they deposit small amounts of radiation along their entire path and continue beyond the tumor, exposing surrounding healthy tissue [25].
- **Protons**; Proton beams consist of positively charged particles generated by cyclotrons or synchrotrons. Like photons, they can reach deep tumors, but they have a different physical property: they deposit most of their energy at a specific depth, reaching the Bragg peak, and then stop. This allows for a more precise delivery of radiation to the tumor while sparing tissues beyond it. Nevertheless, the large size and high cost of proton facilities still limit their availability [9], [24], [25].
- **Electrons:** Electron beams are commonly applied in routine clinical practice. Their penetration in tissue is limited, which makes them particularly useful for treating tumors located close to the surface, such as skin cancers or superficial lymph nodes [9], [24], [25]
- **Neutrons**: Neutron beams are produced in neutron generators or cyclotrons, where protons are accelerated and directed onto a suitable target to release neutrons. They are

characterized by a high LET, causing dense ionization tracks and more severe DNA damage compared to photons. Its clinical use is limited due to technical challenges and the complexity of building dedicated facilities [9], [24], [25].

1.3.2 Brachytherapy

Brachytherapy is a form of radiation therapy in which small sealed radioactive sources are placed inside or very close to the loclalized tumor, either through direct implantation or with catheters. Its main advantage is the ability to deliver a high radiation dose directly to the tumor, while limiting exposure to surrounding healthy tissues, since the radiation does not need to pass through the skin or other organs [27]. In this way, it provides better protection of normal structures compared with EBRT. The isotopes most commonly used are iodine-125 and palladium-103.
Another advantage is the shorter treatment schedule, as brachytherapy can often be completed in just a few days, unlike EBRT which usually requires several weeks [27].
EBRT and brachytherapy are important for localized prostate cancer, but they are not suitable for metastases. EBRT needs large machines and is usually limited to local treatment or to relieve symptoms from single lesions.
Brachytherapy requires an invasive procedure to place radioactive sources inside the prostate and cannot be used for metastatic disease. Because of these limits, more attention is now given to radiopharmaceuticals in targeted radionuclide therapy (TRT). This is a systemic treatment: after intravenous injection, the drug travels through the whole body and can reach and treat metastatic sites that local radiation cannot cover.

1.4 Nuclear Medicine and Radiopharmaceuticals

Nuclear medicine is defined as the application of radionuclides to medicine. Nuclear medicine takes advantage of the unique properties of radioactive elements, which have significantly different physical properties compared to stable elements but identical chemical behavior. More specifically, radionuclides decay at a characteristic rate (half-life) emitting particles (such as α, β^-, or positrons) or electromagnetic radiation (γ rays) [20].
In this context, radioactive elements are administered as radiopharmaceuticals. These compounds are made for medical use, where the radionuclide is attached to a biologically active carrier. The carrier, which can be a small molecule, a drug or even blood cells, brings the radionuclide to a specific organ or tissue. In this way, radiopharmaceuticals serve two main purposes: they can be used either for diagnostic imaging or for delivering targeted radiation to treat specific diseased organs. In some cases, the same molecular carrier can be labeled with different radionuclides for both applications, forming theranostic pairs that enable personalized diagnosis and therapy [28].

1.4.1 Radionuclide imagining

Ionizing radiation from radionuclides in radiopharmaceuticals can be detected with imaging devices such as gamma cameras, Single Photon Emission Computed Tomography (SPECT), and Positron Emission Tomography (PET) scanners [29]. SPECT is used to detect radionuclides that emit single gamma rays, while PET detects the two photons produced after positron annihilation [28]. These techniques allow the study of physiological and molecular processes in a noninvasive way [20].

Table 1.2 summarizes the main radionuclides commonly employed in PET and SPECT imaging, together with their emission type and half-life.
In both clinical practice and research, nuclear medicine relies on radiopharmaceuticals administered orally, intravenously or by inhalation to visualize different organs [28]. Diagnostic images are generated from the emitted radiation and reconstructed by the camera into computer-processed images that can reveal possible abnormalities [20], [28].

Table 1.2: Physical characteristics of radionuclides commonly used in PET and SPECT imaging. Adapted from [20].

PET			**SPECT**		
Nuclide	**Emission**	**Half life**	**Nuclide**	**Emission**	**Half life**
^{11}C	β^+	20.36 min	^{111}In	ε	2.80 d
^{18}F	β^+	109.77 min	^{99m}Tc	IT	6 h
^{52}Fe	$\varepsilon + \beta^+$	8.73 h	^{67}Ga	ε	3.26 d
^{89}Zr	$\varepsilon + \beta^+$	78.4 h	^{123}I	ε	13.22 h

In PET imaging, one of the most widely used radionuclides is fluorine-18 (^{18}F), which has a half-life of about 110 minutes and can be incorporated into biologically active molecules such as ^{18}F-fluoro-2-deoxyglucose (FDG). After injection into the patient, the radionuclide decays by emitting a positron. When the positron slows down and reaches the end of its short range, it encounters an electron. Because positrons and electrons are antiparticles, they annihilate, converting their mass into two photons of 511 keV emitted in opposite directions, 180° apart [20], [28].

$$^{18}_{9}F \rightarrow {}^{18}_{8}O + e^+ + \nu_e \qquad (1.16)$$

The PET scanner detects these pairs of photons using rings of detectors surrounding the patient. Each detector module contains a scintillation crystal coupled to a photodetector. When a photon hits the crystal, the energy is absorbed and converted into flashes of visible light. The intensity of the light is proportional to the photon energy, and the photodetector converts this light into an electrical signal. By detecting two photons at the same time (coincidence detection), the scanner determines the line along which the annihilation occurred, known as the line of response (LOR) [20], [28]. Modern PET systems record many of these LORs from different angles. To obtain a whole-body scan, the patient table moves step by step through the scanner, with several minutes of acquisition at each position. The individual images are then merged together to form a single continuous 3D image of the body [20].
Single Photon Emission Computed Tomography (SPECT) is a nuclear imaging technique that detects the γ photons emitted directly by radionuclides. In a typical clinical system, rotating gamma cameras acquire projection images from many different angles around the patient. These raw data consist of one dimensional projections of the emitted radiation, which are then mathematically reconstructed into cross sectional images. A standard SPECT scan usually takes 20–30 minutes and involves 60–120 projections over 180° for cardiac studies or 360° for other regions. Although its spatial resolution and quantitative accuracy are lower than PET. SPECT has the advantage of allowing multi radionuclide imaging, since photons of different energies can be distinguished and recorded simultaneously [28], [30].

1.4.2 Targeted radionuclide Therapy

Minimal residual disease and micrometastatic spread remain a major therapeutic challenge, since conventional approaches such as surgery or EBRT lose efficacy once cancer has disseminated [31]. TRT offers a promising solution by using radiolabeled molecules such as antibodies, antibody fragments, peptides or small ligands conjugated to therapeutic radionuclides that emit Auger electrons (AE), α-particles or β-particles [21]. These radiopharmaceuticals selectively deliver cytotoxic radiation to tumor cells, enabling the treatment of inoperable or widespread disease while limiting damage to surrounding healthy tissues [21], [31].

1.4.2.1 α and β^- emitters

Alpha particles are highly energetic, with emission energies in the range of 5–9 MeV, but travel only a very short distance in tissue, typically 50–100 μm, which corresponds to just a few cell diameters. Their LET is high, typically around 80 keV/μm along most of their track and increases sharply towards the end of the path, where the Bragg peak occurs, reaching values close to 300 keV/μm [21]. This means that α particles deposit large amounts of energy in a small volume, creating dense clusters of DNA damage that are extremely difficult for cells to repair. As a result, they are highly cytotoxic and can efficiently kill single tumor cells or small clusters, making them particularly suitable for eliminating minimal residual disease and micrometastases [21], [32].

The therapeutic effect depends not only on the probability that an α particle crosses the cell nucleus but also on Bystander and Crossfire Effects [32]. As it can be noticed in figure 1.8, α particles travel only a few cell diameters while β particles have a much longer range in tissue, on the order of millimeters, leading to the so called Crossfire Effect. This effect allows radiation from one decaying atom to reach nearby tumor cells, compensating for heterogeneous uptake and reducing the need to target every single cell [21], [32].

Overall, their ability to penetrate deeper into tissue makes β particle emitters particularly effective against larger or more diffuse tumor masses, in contrast to the short range damage caused by α particles [20].

The table below provides the main α and β emitting radionuclides used in TRT:

Table 1.3: Examples of radionuclides explored for therapy. Adapted from [20].

Nuclide	Emission	Half-life (days)	Emax (MeV)	Mean range (mm)
Astatine-211	α	0.33	5.87	0.04-0.1
Radium-223	α	11.4	5.78	0.04-0.1
Lutetium-177	β	6.7	0.50	0.28
Iodine-131	β	8.0	0.81	0.40
Yttrium-90	β	2.7	2.30	2.76
Copper-67	β	2.6	0.57	0.60

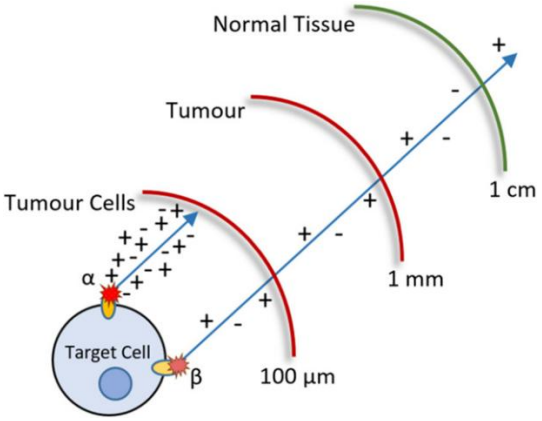

Figure 1.8: Path length of alpha and beta radiation. The high LET of alpha-particle radiation is associated with a high density of ionisation events. Adapted from [33].

1.4.2.2 Auger electrons

Auger electrons (AEs) are very low energy electrons released when certain radionuclides decay through electron capture (EC) or internal conversion (IC). These processes leave a vacancy in the inner electron shells, which is filled by electrons from higher shells. The excess energy is then either emitted as an X-ray or transferred to another electron that is ejected as an AE [34]. A single EC or IC decay can trigger a cascade of electronic transitions that generates roughly 5–30 AEs, with energies ranging from just a few electronvolts to several kiloelectronvolts [35]. AEs are unique because of their extremely short range in biological tissue. Most travel only a few nanometres, which is on the order of the size of DNA itself (~2 nm). Higher energy electrons from K-shell transitions may go further, but still only tens of nanometres [34].

This very short path length gives AEs a LET, typically in the range of 1–23 keV/µm, which means that they deposit a large amount of energy per unit distance travelled [35]. Because of this, if an Auger emitter decays close to DNA, the deposited energy is concentrated in a very small volume as it is shown in figure 1.9, producing clustered DNA lesions such as double strand break (DSB). In fact, the energy deposited within 1–2 nm of the decay site can reach values as high as 1 MGy per disintegration, which explains why these electrons can be so lethal for cells [34].

Besides this direct damage to DNA, Auger emitters can also trigger important indirect effects. The ionization of surrounding molecules, particularly water, generates reactive oxygen species (ROS) which can diffuse and further damage DNA and other cellular structures [35].

Moreover, Auger electrons contribute to Bystander Effects, where signals released by irradiated cells induce damage or death in neighboring non irradiated cells, and to a limited form of Crossfire Effect, in which very short range electrons still affect adjacent cells or subcellular structures [21], [35]. Several radionuclides widely used in nuclear medicine are AEs, including technetium-99m, indium-111, iodine-123, and thallium-201 [35]. Their therapeutic potential comes from the ability to deliver very high radiation doses exactly where they are needed, either in the DNA or the cell membrane, while sparing surrounding healthy tissues.

In addition, many AEs also give off γ-rays, making them suitable theranostic agents that combine molecular imaging and targeted cancer therapy [21].

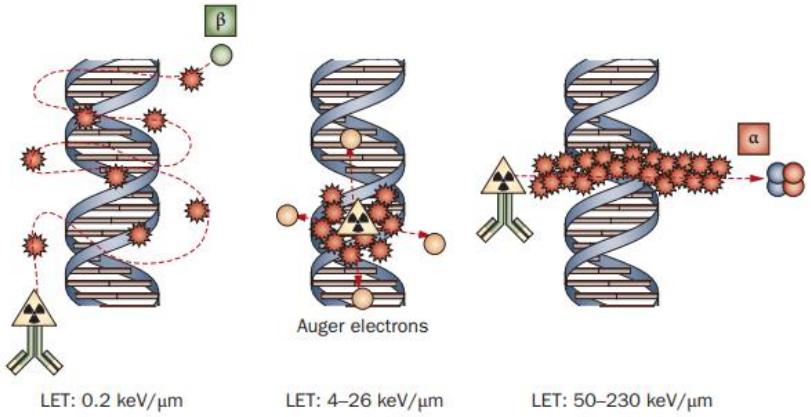

Figure 1.9: Patterns of cellular damage caused by radiation sorted by LET. Adapted from [33].

1.5 Properties of Indium-111 and application in nuclear medicine

Indium-111 is a cyclotron-produced radionuclide with a physical half-life of approximately 67.3 hours, which makes it well suited for labeling biomolecules that circulate in the body for several days, such as antibodies. It decays by EC to stable Cadmium-111 (figure 1.10) and emits two main γ photons at 171 keV and 245 keV energies that can be detected with SPECT cameras [23]. Along with these photons, the decay also produces low energy AEs with very short ranges (<1 µm), which can contribute to local radiation dose and potentially DNA damage if the radionuclide is internalized [37].

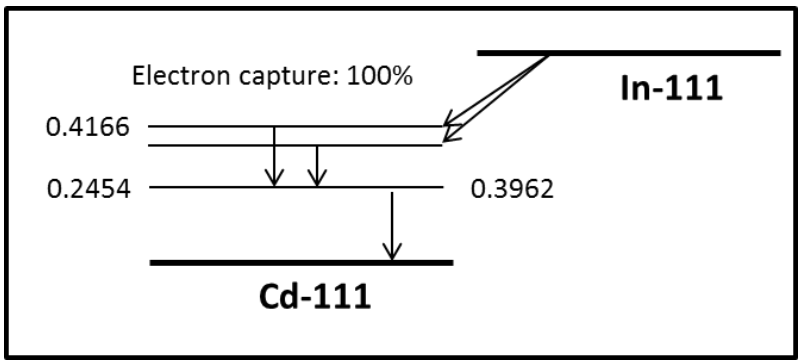

Figure 1.10: Radioactive decay of Indium-111. Adapted from [38].

From a chemical point of view, Indium is a p-block element belonging to Group 13 of the periodic table, with the electronic configuration $[Kr]4d^{10}5s^{2}5p^{1}$. In biological conditions, it is stable in the oxidation state In(III) behaving as a hard Lewis acid with high charge density and a preference for oxygen and nitrogen donor atoms [20], [37].
Its relatively large ionic radius (≈0.8 Å) allows high coordination numbers, typically 7–9, which require chelators capable of offering multiple donor atoms. Polydentate chelators such as diethylenetriaminepentaacetic acid (DTPA), 1,4,7,10-tetraazacyclododecane-1,4,7,10-tetraacetic acid (DOTA) and 1,4,7-triazacyclononane-1,4,7-triacetic acid (NOTA) are widely used to form highly stable Indium complexes with excellent in vivo kinetic stability [20], [37].

The choice of chelator is critical: it must ensure efficient binding to In(III), high molar activity, and prevent demetallation that could lead to the unwanted accumulation of free radiometal in healthy tissues.
DTPA can rapidly form stable complexes with Indium-111 at room temperature, which makes it ideal for labeling thermosensitive biomolecules such as antibodies or peptides [37].
In contrast, DOTA provides greater in-vivo stability but requires heating to form a stable complex, a limitation for heat labile compounds.
Because of these characteristics, DTPA-based chelators are the most commonly employed for Indium-111 labeling, particularly in FDA approved radiopharmaceuticals [20], [37]. Clinically, Indium-111 has been widely used in immuno-SPECT imaging, where antibodies or peptides are labeled via bifunctional chelators. Examples include FDA approved radiopharmaceuticals such as ProstaScint ([^{111}In]In-capromab pendetide) for prostate cancer imaging, OncoScint ([^{111}In]In-satumomab pendetide) for colorectal and ovarian cancers, and MyoScint ([^{111}In]In-imciromab) for myocardial infarction [37]. In addition, [^{111}In]In-octreotide is an important ^{111}In-labeled peptide used for the imaging of neuroendocrine tumors [20].

1.6 Radiopharmaceuticals for prostate cancer

1.6.1 PSMA targeting

One of the most important targets for prostate cancer imaging and therapy is prostate-specific membrane antigen (PSMA), also known as NAALADase, glutamate carboxypeptidase II or folate hydrolase. PSMA is a type II membrane glycoprotein of about 100 kDa, with a short intracellular tail, a single transmembrane segment and a large extracellular domain containing the active site with two zinc ions, responsible for its enzymatic function [7]. Discovered in 1987 as a novel antigenic marker in prostate cancer cells, PSMA is overexpressed in 90–100% of prostate cancers, with levels increasing in advanced and hormone-resistant tumors. This makes it an excellent target for molecular imaging and targeted radionuclide therapy.
Radiolabeled PSMA tracers can be tagged with different radionuclides such as Ga-68 for PET imaging or Lutetium-177 and Actinium-225 for therapy and when injected intravenously, they accumulate specifically at tumor sites thanks to PSMA binding [39].
Although called “prostate-specific,” PSMA is also found, at lower levels, in normal prostate epithelium, salivary glands, proximal renal tubules, small intestine, certain neural ganglia and in the neovasculature of several solid tumors [40], [41]. This expression pattern explains both the clinical utility and the main safety concerns of PSMA targeted agents.
Over the past decade, a wide range of PSMA targeted ligands has been systematically developed and optimized for radiopharmaceutical applications. Two main strategies have emerged for targeting PSMA. The first exploits the macromolecular protein structure of PSMA to design monoclonal antibodies and antibody derived molecules, such as J591, that recognize extracellular epitopes of the antigen [40]. The second, more widely adopted approach, leverages the enzymatic activity of PSMA by using small molecule enzyme inhibitors or binding agents as targeting vectors [7].
Small molecule PSMA inhibitors are zinc binding compounds typically linked to glutamate or its analogs and can be categorized into three major families: (1) phosphorus based compounds, (2) thiols and (3) ureas [7], [41]. Among these, the urea based ligands have proven to be the most effective and are now the foundation of modern PSMA-targeted imaging and therapy. These urea-based inhibitors share a modular design composed of three key components as it shows in figure 1.11:
(i) a binding motif, classically glutamate–urea–lysine (Glu–urea–Lys), which binds to the zinc containing active site of PSMA;

(ii) a linker, which modulates pharmacokinetic behavior and biodistribution;
(iii) a radiolabel-bearing moiety, such as a chelator (DOTA or 1,4,7,10-tetraazacyclododecane-1-glutaric acid-4,7,10-triacetic acid (DOTAGA)) for radiometal labeling, or a prosthetic group for labeling with non-metallic isotopes such as fluorine, iodine, or astatine [7], [21].

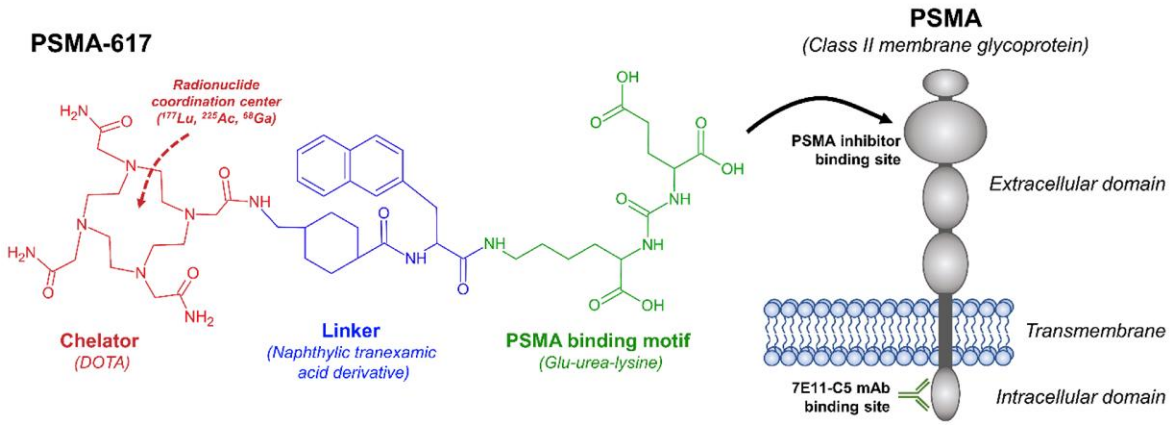

Figure 1.11: Structural components of PSMA-617 and its interaction with the PSMA receptor. The molecule consists of three main parts: a chelator (DOTA) for radiometal binding, a linker (naphthylic tranexamic acid derivative) that modulates pharmacokinetics, and a PSMA-binding motif (Glu-urea-Lys) that targets the enzymatic site on the extracellular domain of PSMA. Adapted from [42].

The first Glu–urea–Lys–based small molecule inhibitors, [^{123}I]I-MIP-1072 and [^{123}I]I-MIP-1095, were introduced clinically in 2008 for prostate cancer imaging [7]. These tracers showed rapid and specific localization in tumor lesions, including soft-tissue and bone metastases [7], [39]. Their success led to further development of second-generation inhibitors such as MIP-1404, and eventually to the creation of today's widely used theranostic ligands PSMA-617, PSMA-I&T and PET tracers like PSMA-116 [7], [40], [41], [42]
PSMA ligands can carry different therapeutic emissions:

- **β-emitters:** e.g. [^{177}Lu]Lu-PSMA-617 is a theranostic agent in which Lutetium-177 decay produces both tumor-killing β^- particles and imageable γ photons. This dual emission enables simultaneous therapy and imaging, allowing clinicians to visualize tracer distribution and tumor uptake through planar scintigraphy or SPECT imaging [40]. Lutetium-177 emits β particles with relatively low energy (mean 137 keV) and a short penetration range in soft tissues (minimun 0.7 mm, maximum 2.1 mm), providing precise, localized irradiation of tumor lesions. It also has a moderate half-life of 6.6 days, which facilitates both effective radiation delivery and practical handling in clinical use [42]. Clinical studies have demonstrated that [^{177}Lu]Lu-PSMA-617 achieves meaningful PSA reductions and clinical responses in men with advanced prostate cancer, with hematologic and salivary toxicities that are generally mild and manageable [40], [41].
- **α-emitters**: Clinical studies with [^{225}Ac]Ac-PSMA-617 have shown impressive PSA reductions and tumor responses in advanced prostate cancer [39], [42]. Actinium-225 has gained major interest for PSMA-targeted treatments [40]. Alpha particles have very high energy (5–8 MeV) and an extremely short range in tissue, allowing strong, localized DNA damage and effective tumor killing while limiting exposure to nearby healthy cells [39], [40]. Actinium-225 has a half-life of about 10 days and emits four α particles during decay, giving it high cytotoxic potential even at low doses. However,

the same properties that make α therapy powerful can also cause irreversible toxicity, particularly xerostomia from salivary gland damage. Bone marrow toxicity is lower than with β emitters like Lutetium-177 due to the short penetration of α particles [24], [25]. Overall, [^{225}Ac]Ac-PSMA-617 is a highly potent option, but minimizing side effects remains a key challenge [39], [40], [42].

- **Auger/conversion-electron emitters**: Terbium-161 has emerged as a promising alternative respect to Lutetium-177 for PSMA-targeted therapy [39]. With its very short radiation path, ranging from just a few nanometers to micrometers Terbium-161 is particularly effective when it localizes near the cell nucleus or DNA. By emitting both β particles and numerous low energy electrons, it can induce greater DNA damage and achieve stronger tumor cell killing [7], [39]. Preclinical studies have shown that [^{161}Tb]Tb-PSMA-617 can be up to three times more effective than, maintaining similar pharmacokinetic and biodistribution profiles [7].

In addition to these challenges, conventional PSMA-targeted agents exhibit high renal uptake and rapid clearance from the bloodstream. This combination reduces tumor retention and therapeutic efficacy while increasing the radiation burden to the kidneys and salivary glands. Consequently, recent research has focused on improving their pharmacokinetic profile by extending circulation time and reducing renal reabsorption. Among these approaches, heterobivalent radioligands have emerged as a promising strategy to enhance tumor accumulation and minimize off-target toxicity [39], [43].

1.6.2 Heterobivalent radioligands

Heterobivalent ligands that combine a PSMA-binding unit with an albumin-binding domain have recently gained attention as a strategy to improve PSMA-targeted radiopharmaceuticals. These agents can temporarily bind to circulating albumin, allowing them to stay longer in the bloodstream. This extended circulation time helps increase tumor uptake and retention while lowering radiation exposure to healthy tissues such as the kidneys and salivary glands. Because prostate tumors often show variable PSMA expression, this dual-target approach aims to provide more consistent therapeutic effects and improved safety compared to traditional PSMA only tracers [39], [43].

1.6.2.1 Albumin binding domain

Human serum albumin is the most abundant protein in the blood, with a molecular weight of about 66.5 kDa and a circulation time of around 19 days. Because of this long half-life, attaching a reversible albumin-binding group to a PSMA ligand allows the tracer to bind temporarily to albumin, stay longer in the bloodstream, and reach tumors more efficiently [44]. The goal is to extend the circulation time to enhance tumor uptake and retention, enabling administration of a lower activity while maintaining efficacy and potentially reducing exposure to healthy tissues. This is important because typical small molecule PSMA tracers often accumulate in the salivary glands and kidneys.
With β emitters, this can lead to xerostomia and, in patients who have undergone multiple treatments, some bone marrow toxicity; with α emitters, xerostomia can even become dose-limiting.
Extending the time, the tracer stays in the bloodstream through albumin binding offers a way to increase the tumor dose without raising the injected activity [39], [43]. Early evidence came from folate radioconjugates, where adding an albumin-binding group extended the blood half-life and tripled tumor uptake compared with the non albumin-binding version. In particular, Müller and co-workers demonstrated this principle with the folate ligand [^{177}Lu]Lu-cm09,

which showed a threefold higher tumor uptake and a 2.5 fold lower kidney uptake compared with its non albumin binding analogue [^{177}Lu]Lu-EC0800 [45]. These results demonstrated that albumin binding can beneficially alter biodistribution and encouraged the application of the same strategy to PSMA ligands. A key albumin-binding group used in PSMA ligands is 4-(p-iodophenyl)butyric acid (IPBA). This small, reversible moiety can be easily attached to urea-based scaffolds. Studies across different IPBA–PSMA tracers consistently show two main trends: (i) prolonged circulation leading to higher tumor uptake and retention and (ii) trade-offs involving increased kidney, and occasionally bone marrow, exposure.
These results highlight the need to carefully balance albumin-binding strength and linker design [39], [43], [44]. For example, HTK01169 (IPBA–Glu-urea-Lys) achieved a much higher tumor dose than [^{177}Lu]PSMA-617 but also caused a substantially greater kidney dose, highlighting the need to adjust albumin affinity and improve linker design [43], [46].
Umbricht and colleagues compared two PSMA ligands with different albumin-binding strengths: ALB-53, which includes the strong binder IPBA, and ALB-56, which carries the weaker p-tolyl group. Even with its lower affinity for albumin, [^{177}Lu]Lu-PSMA-ALB-56 cleared more quickly from non target tissues, showed less kidney retention, and reached a tumor-to-kidney ratio about three times higher than [^{177}Lu]Lu-PSMA-ALB-53. In treatment studies, [^{177}Lu]Lu-PSMA-ALB-56 extended survival and produced complete remissions in several mice, suggesting that moderate albumin binding offers a better balance between tumor uptake and normal-tissue exposure [26] Overall, IPBA has become one of the most effective albumin-binding groups for PSMA heterobivalent ligands, as it is compact, metabolically stable and shows reliable albumin binding.

1.7 Thesis aim and Outline

Prostate cancer is one of the most common cancers in men and remains a leading cause of cancer-related deaths worldwide. In recent years, targeted radiopharmaceuticals have become important tools to improve both the diagnosis and treatment of this disease. These agents can combine imaging and therapy in a single compound, known as theranostic agents. This strategy allows a more personalized and effective management of patients by enabling precise tumor detection, better prediction of treatment response and easier monitoring of therapy. Among the different molecular targets studied for prostate cancer, PSMA has proven to be one of the most promising.
Radioligands that target PSMA, such as [^{177}Lu]Lu–PSMA–617, have achieved excellent clinical results. However, these compounds often show fast clearance from the bloodstream and unwanted uptake in healthy organs like the kidneys and salivary glands. This behavior can lower their therapeutic effectiveness and increase the risk of side effects. For this reason, improving the *in vivo* stability and tumor retention of PSMA-targeted radiopharmaceuticals remains an important goal for the development of next generation agents.
In this context, the main goal of this thesis is the design, synthesis, radiolabeling, and preliminary biological evaluation of a novel PSMA-targeted radioconjugate bearing an albumin-binding domain, aim at improving the pharmacokinetic profile and tumor accumulation of PSMA ligands.
The structure of the thesis is organized as follows:

- **Chapter 1** presents an overview of prostate cancer and PSMA-targeted radiopharmaceuticals, explaining the motivation for introducing albumin-binding domains and heterobivalent design strategies to improve pharmacokinetic and therapeutic properties.

- **Chapter 2** describes the materials and methods used for the synthesis of both non-radioactive and radioactive compounds, as well as the experimental procedures for *in vitro* and *in vivo* evaluations, including biodistribution studies and small animal μSPECT/CT imaging.
- **Chapter 3** reports and discusses the obtained results, highlighting the chemical and radiochemical characterization, the *in vitro* cell studies (FLU, PC3-PIP, and 2-PMPA inhibition assay), as well as the protein-binding and biodistribution data. These results, together with the μSPECT/CT imaging, demonstrate the effect of the albumin-binding domain on the pharmacokinetic behavior and tumor targeting efficiency of the new conjugate.
- **Chapter 4** presents the main conclusions and future perspectives, emphasizing how this approach may contribute to the development of improved PSMA-targeted radiopharmaceuticals for prostate cancer theranostics.

Chapter 2

Materials and Methods

2.1 Solvents and reagents

All reactions were carried out in a ventilated chemical fume hood at room temperature, using dry solvents when required. Unless otherwise stated, all chemicals and solvents were reagent grade and used without further purification, reagents were obtained from Sigma-Aldrich (St. Louis, MO, USA), unless otherwise specified:

- ACN, Acetonitrile
- Boc–NH–PEG(3)–NH_2·HCl, tert-Butoxycarbonylamino-poly(ethylene glycol)-3-amino hydrochloride
- DCM (CH_2Cl_2), Dichloromethane
- DIPEA, N,N-diisopropylethylamine
- DMF, N,N-Dimethylformamide
- DOTA (1,4,7,10-tetraazacyclododecane-1,4,7,10-tetraacetic acid) previously synthesized according to the procedure reported in Santos et al. [51]
- HBTU, O-(benzotriazol-1-yl)-N,N,N',N'-tetramethyluronium hexafluorophosphate
- IPBA, 4-(p-Iodophenyl)butyric acid
- MeOH, Methanol
- N-Fmoc-tranexamic acid, amine-protected derivative of tranexamic acid
- Piperidine
- PSMA–$(tBu)_3$, tert-butyl-protected PSMA derivative, previously prepared according to the procedure reported in Santos et al. [51]
- THF, Tetrahydrofuran
- TFA, Trifluoroacetic acid
- [^{111}In]$InCl_3$ (370 MBq/mL in HCl) obtained from Curium (Netherlands B.V.)

2.2 Purification and characterization methods

2.2.1 Solid Phase Extraction

Solid-phase extraction (SPE) was used for the purification and concentration of the samples. This method enables the selective isolation of the desired compounds through interactions between the analytes in solution and the solid sorbent material within the cartridge. Purification was carried out using Sep-Pak Vac 6 cc C18 (500 mg), Sep-Pak Vac 12 cc C18 (2 g), and Sep-Pak C18 Plus Light cartridges (Waters), all packed with porous chromatographic material.

The solid-phase extraction procedure is illustrated in figure 2.12. The cartridges were first conditioned and equilibrated with appropriate solvents, followed by sample loading. After washing to remove impurities, the analytes were eluted using increasing concentrations of ACN containing 0.1% of TFA.

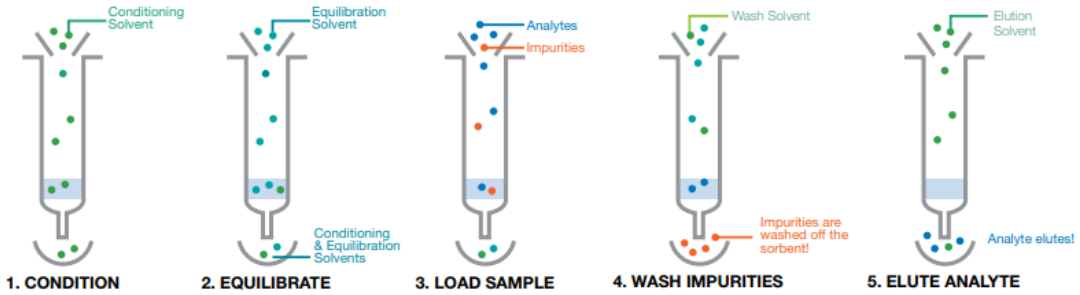

Figure 2.12: Main steps of the solid-phase extraction procedure. Adapted from [47].

2.2.2 Thin-Layer Chromatography

Thin-layer chromatography (TLC) was carried out on silica gel plates coated with a fluorescent indicator F254 (Merck). The spots were visualized under UV light at 254 nm. TLC was used to monitor the progress of the reactions and to check the fractions collected from the silica gel column chromatography.

2.2.3 Column Chromatography

Silica gel column chromatography was used to purify some of the synthesized compounds, following the typical workflow illustrated in figure 2.13. Silica gel 60 Å (70–230 mesh, ASTM; Merck) was used as the stationary phase and packed into glass columns of suitable size, equilibrated with the selected solvent system. The eluent composition was chosen according to the polarity and chemical properties of each compound, while the column dimensions depended on the amount of material to be purified. Samples were loaded onto the top of the column and eluted by gravity, collecting the eluate in small fractions. Fractions were monitored by TLC, and those containing the desired product were combined, concentrated under reduced pressure, and dried. The purified compounds were finally characterized by standard analytical techniques.

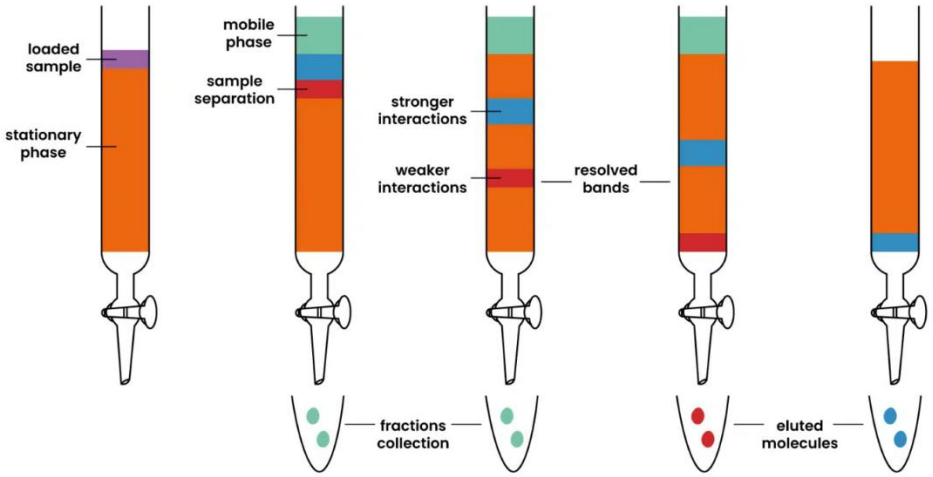

Figure 2.13: Schematic representation of the column chromatography. Adapted from [48].

2.2.4 High Performance Liquid Chromatografy

High-Performance Liquid Chromatography (HPLC) is an analytical technique used to separate, identify, and quantify the components of a mixture. An HPLC system is composed of one or more pumps, an injector or autosampler, a chromatographic column, a detector and data acquisition software. The column, considered the heart of the system, is packed with solid particles that compose the stationary phase, where the separation of compounds takes place. The mobile phase, consisting of a solvent or a mixture of solvents, is pumped through the column at high pressure, carrying the analytes that interact differently with the stationary phase, depending on their chemical and physical properties. These differences lead to specific retention times, allowing the identification and quantification of the substances in the sample.
In reversed phase chromatography, the stationary phase is nonpolar (for example, C18), while the mobile phase is more polar. As a result, less polar molecules interact more strongly with the stationary phase and are eluted more slowly. The detector continuously monitors the effluent leaving the column and converts the signal into a chromatogram, which provides both qualitative and quantitative information about the analyzed sample [49]. HPLC analyses were performed using HPLC-grade solvents and double-distilled water, which was filtered through 0.22 µm membrane filters to ensure purity. Different systems and analytical methods were employed:

- Analytical HPLC analyses and compound purifications were carried out on PerkinElmer Series 200 analytical HPLC instrument (figure 2.14), equipped with a UV−visdetector (Series 200 UV/VIS Detector**)** with a Supelco Analytical Discovery BIO Wide Pore C18_5 column (250mm×4.6mm, 300 Å poresize, 5 µm particle size) with a flow rate of 1mL/min. HPLC solvents consisted of 0.1% TFA in water (eluent A) and 0.1% TFA in ACN (eluent B):

Figure 2.14: PerkinElmer Series 200 analytical HPLC system equipped with a UV–vis detector (Series 200 UV/VIS Detector) and a Supelco Discovery BIO Wide Pore C18 column (250 × 4.6 mm, 300 Å, 5 µm).

- Analytical HPLC analyses were also performed on a PerkinElmer Flexar analytical HPLC system (figure 2.15), coupled to a PerkinElmer Flexar UV/Vis detector and a LabLogic Flow-RAM gamma detector, using an EC 250/4 Nucleosil 100–10 C18 column (Macherey-Nagel; REF 720023.40, 250 × 4 mm, 100 Å pore size, 5 µm particle size) at a flow rate of 1 mL/min. The mobile phase consisted of 0.1% TFA in water (eluent A) and 0.1% TFA in ACN (eluent B). Both UV absorbance and γ-radiation were continuously monitored.

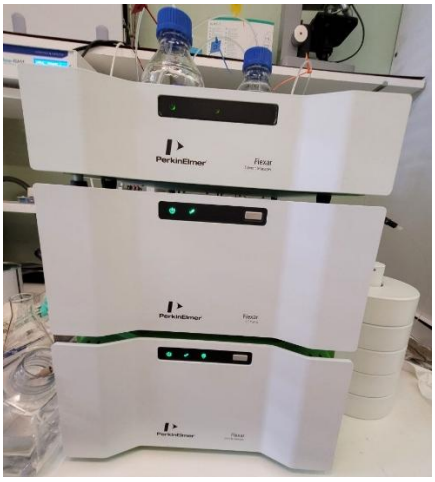

Figure 2.15: PerkinElmer Flexar HPLC system coupled with a UV/Vis detector and a LabLogic Flow-RAM gamma detector used for radiometric analyses.

Analytical methods:

Method A

Analytical system: UV/Vis

Column: Supelco Analytical Discovery BIO Wide Pore C18_5 (250 × 4.6 mm, 300 Å pore size, 5 µm particle size)

Eluents: A – 0.1% TFA in water; B – 0.1% TFA in ACN

Flow rate: 1 mL/min

Detenction: 220 nm

Step	Time (min)	Eluent A (%)	Eluent B (%)	Curve
0	0	95	5	0
1	25	0	100	1
2	2	0	100	0
3	1	95	5	1
4	2	95	5	0

Method B

Analytical system: UV/Vis

Column: Supelco Analytical Discovery BIO Wide Pore C18_5 (250 × 4.6 mm, 300 Å pore size, 5 µm particle size)

Eluents: A – 0.1% TFA in water; B – 0.1% TFA in ACN

Flow rate: 1 mL/min

Detenction: 220 nm

Step	Time (min)	Eluent A (%)	Eluent B (%)	Curve
0	0	70	30	0
1	20	30	70	1

Method C

Analytical system: UV/Vis

Column: Supelco Analytical Discovery BIO Wide Pore C18_5 (250 × 4.6 mm, 300 Å pore size, 5 µm particle size)

Eluents: A – 0.1% TFA in water; B – 0.1% TFA in ACN

Flow rate: 1 mL/min

Detenction: 220 nm

Step	Time (min)	Eluent A (%)	Eluent B (%)	Curve
0	0	70	30	0
1	15	30	70	1

Method D

Analytical system: Radiometric

Column: EC 250/4 Nucleosil 100–10 C18 (Macherey-Nagel; 250 × 4 mm, 300 Å pore size, 5 µm particle size)

Eluents: A – 0.1% TFA in water; B – 0.1% TFA in ACN

Flow rate: 1 mL/min

Detenction: 254 nm and γ-detection

Step	Time (min)	Eluent A (%)	Eluent B (%)	Curve
0	0	95	5	0
1	25	0	100	1
2	2	0	100	0
3	1	95	5	1
4	2	95	5	0

2.2.5 Electrospray Ionization Mass Spectrometry (ESI-MS)

Electrospray ionization mass spectrometry (ESI-MS) is an analytical technique that allows the qualitative and quantitative characterization of analyte molecules through their conversion into ions. During the process, electrical energy promotes the transfer of ions from solution to the gas phase, allowing the analysis of both ionic and neutral compounds after protonation or cationization. The technique involves the formation of a fine spray of charged droplets under high voltage, followed by solvent evaporation and the release of ions into the gas phase. These ions are then directed into the mass analyser, where they are separated according to their mass to charge (m/z) ratio, generating a spectrum that reflects their relative abundance. ESI-MS combines high sensitivity with the ability to analyse non volatile and thermally labile compounds, making it a reliable tool for molecular identification [50].

In this study, high-resolution ESI mass spectra in positive ion mode were acquired using a QqTOF Compact mass spectrometer (Bruker Daltonics). The TOF analyser was calibrated using a Tune Mix calibration solution (Agilent). Data acquisition and processing were performed with Compass DataAnalysis 6.1 software. Samples collected from HPLC purification (ACN/water mixtures) were diluted in ACN to a final concentration of approximately 1×10^{-6} M and directly injected into the spectrometer.

2.3 Chemical Synthesis and Characterization of Non-radioactive Compounds

2.3.1 Synthesys of protected PSMA-binding motif, PSMA–(tBu)$_3$: di-tert-butyl ((6-(2-(4-(aminomethyl)cyclohexane-1-carboxamido)-3-(naphthalen-2-yl)propanamido)-1-(tert-butoxy)-1-oxohexan-2-yl)carbamoyl)glutamate

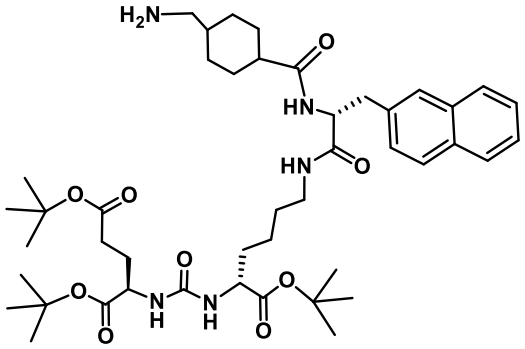

N-Fmoc-tranexamic acid (74.3 mg, 0.195 mmol) was dissolved in dry DMF (5 mL) together with HBTU (72.5 mg, 0.195 mmol) and DIPEA (88 µL, 0.5 mmol). The activation reaction proceeded for 10 minutes, after which the tBu-protected PSMA precursor, containing a free amine function (57.7 mg, 0.09 mmol), previously prepared according to the procedure reported in [51], was dissolved in dry DMF (5 mL) and added to the reaction mixture. The mixture was stirred for 2 h and monitored by HPLC using Method A to verify the reaction progress (HPLC rt 27.4 min). After 2 h the reaction was complete and the piperidine was added to the solution to remove the Fmoc protecting group; the mixture was stirred for 2 hour and then monitored by HPLC using Method A (rt 21.4 min). After the evaporation of the solvent in the vacuum line, the mixture was purified through the Sep-pak cartridge eluted with a mixture with 0.1% TFA in water and 0.1% TFA in ACN. ACN was removed under a flux of nitrogen. After lyophilization, compound 1 was obtained as white solid (39.9 mg, 54% yield). ESI(+)-MS for $C_{45}H_{69}N_5O_9$: *m/z* calcd for $[M+H]^+$ 824.51, found: 824.7 $[M+H]^+$.

2.3.2 Synthesis of tert-butyl (16-(4-iodophenyl)-13-oxo-3,6,9-trioxa-12-azahexadecyl)carbamate

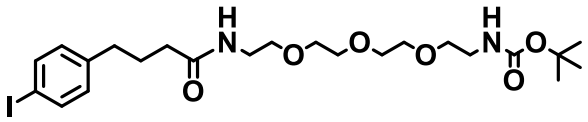

A solution of HBTU (652.29 mg, 1.72 mmol), DIPEA (600 µL, 3.44 mmol) and IPBA (500 mg, 1.72 mmol) in dry DMF (5 mL) was stirred for 10 minutes. After 10 minutes Boc–NH–PEG(3)–NH_2·HCl was added to the previous solution. An additional 600 µL of DIPEA were added to the solution to neutralize the acid (HCl) present. The mixture was stirred overnight and monitored by HPLC using Method A to verify the reaction progress. After the evaporation of the solvent DMF in the vacuum line, the crude was dissolved in DCM and extracted 3/4 times with water. The organic phases were dried with magnesium sulfate $MgSO_4$ and filtered. After evaporation of DCM first in the rotavapor and finally in the vacuum line 1369 mg of crude product were obtained.

2.3.3 Synthesys IPBA–PEG–NH_2: N-(2-(2-(2-(2-aminoethoxy) ethoxy) ethoxy) ethyl)-4-(4-iodophenyl) butanamide

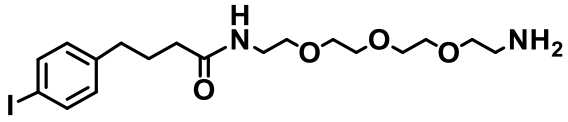

The Boc protecting group was removed with 2 mL of DCM and 0.5 mL of TFA. The mixture was stirred for 1 hour and monitored by HPLC using Method A. The DCM was removed under rotavapor and then through the vacuum line. In order to remove completely the old compound still present, the crude was dissolved in chloroform ($CHCl_3$) and extracted 3 times with H_2O + $NaHCO_3$. The organic phase was then dried with magnesium sulfate ($MgSO_4$) and filtered. The solvent was evaporated in rotavapor and then in vacuum line. After purification, IPBA-PEG-NH_2 was obtained as a white solid (0.778 g, 1.675 mmol, 97% yield). ESI(+)-MS: for the molecular formula $C_{18}H_{29}IN_2O_4$ the *m/z* calcd for $[M + H]^+$:465.12, found: 465.18.

2.3.4 Sinthesys of IPBA–PEG–DOTA–PSMA-$(tBu)_3$-Et: 2-(4,10-bis(2-(tert-butoxy)-2-oxoethyl)-7-(25-(4-iodophenyl)-2,2-dimethyl-4,8,22-trioxo-3,12,15,18-tetraoxa-9,21-diazapentacosan-5-yl)-1,4,7,10-tetraazacyclododecan-1-yl) acetic acid

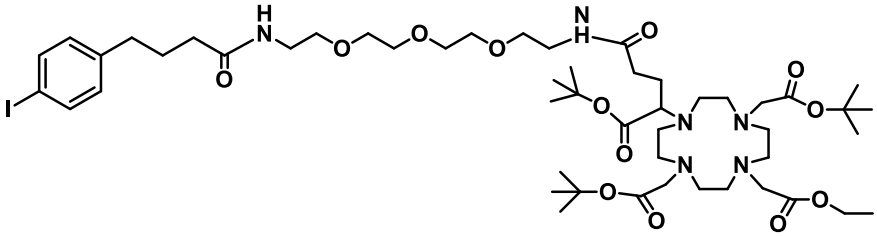

A solution of tBu_3–DOTA monoethyl ester (68 mg, 0.10 mmol), HBTU (38 mg, 0.10 mmol) and DIPEA (50 µL, 0.24 mmol) in dry DMF (2 mL) was stirred at room temperature for 10 minutes. Subsequently, compound IPBA–PEG–NH_2 (56 mg, 0.12 mmol) and an additional amount of DIPEA (30 µL) were added to the reaction mixture. The reaction mixture was stirred overnight, and the progress was monitored by HPLC using Method A. After completion, the solvent was evaporated under reduced pressure, and the crude residue was dissolved in DCM and purified by silica-gel column chromatography (90 % DCM / 10 % MeOH). The purified fractions were analyzed by HPLC using Method A. The combined organic phases were concentrated under vacuum to afford compound IPBA–PEG–DOTA–PSMA-$(tBu)_3$-Et as a yellow oil (52 mg, 0.046 mmol, 46,5% yield). ESI(+)-MS *m/z* calcd for $C_{51}H_{87}IN_6O_{13}$ $[M + H]^+$: 1119.55; found: 1119.62. $[M + 2H]^{2+}$ calcd: 560.28; found: 560.32.

2.3.5 Synthesis of IPBA–PSMA–PEG–DOTA-(tBu)$_3$–COOH: 2-(4,10-bis(2-(tert-butoxy)-2-oxoethyl)-7-(25-(4-iodophenyl)-2,2-dimethyl-4,8,22-trioxo-3,12,15,18-tetraoxa-9,21-diazapentacosan-5-yl)-1,4,7,10-tetraazacyclododecan-1-yl) acetic acid

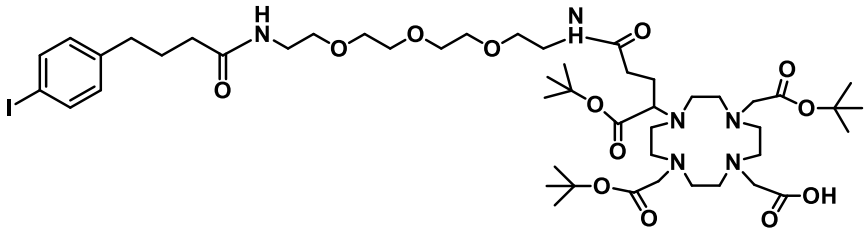

IPBA–PEG–DOTA–PSMA-(tBu)$_3$–Et (52 mg, 0.046 mmol) was dissolved in a mixture of water (1 mL) and THF (1 mL), and a solution of sodium hydroxide NaOH (7.6 mg, 0.19 mmol) previously dissolved in water (90 µL) was added. The mixture was stirred overnight, and the progress of the hydrolysis reaction was monitored by HPLC using Method A. After completion, the reaction mixture was neutralized with HCl and extracted three times with chloroform ($CHCl_3$). The combined organic layers were dried over anhydrous magnesium sulfate ($MgSO_4$), filtered, and the solvent was evaporated under reduced pressure. The resulting residue was dissolved in ACN/water (0.1% TFA) and purified by HPLC with Method B. The collected fractions were combined and lyophilized to afford compound IPBA–PEG–DOTA–PSMA-(tBu)$_3$–COOH as a yellow oil (6.7 mg, 0.00614 mmol, 13% yield). ESI(+)-MS *m/z* calcd for $C_{49}H_{83}IN_6O_{13}$ $[M+H]^+$: 1091.51; found: 1091.61. $[M+2H]^{2+}$ calcd: 546.26; found: 546.32.

2.3.6 Synthesis of IPBA–PEG-DOTA-PSMA -(tBu)$_3$: di-tert-butyl (((2R)-6-((2R)-2-(4-((2-(4,10-bis(2-(tert-butoxy)-2-oxoethyl)-7-(25-(4-iodophenyl)-2,2-dimethyl-4,8,22-trioxo-3,12,15,18-tetraoxa-9,21-diazapentacosan-5-yl)-1,4,7,10-tetraazacyclododecan-1-yl)acetamido)methyl)cyclohexane-1-carboxamido)-3-(naphthalen-2-yl) propanamido)-1-(tert-butoxy)-1-oxohexan-2-yl) carbamoyl)-D-glutamate.

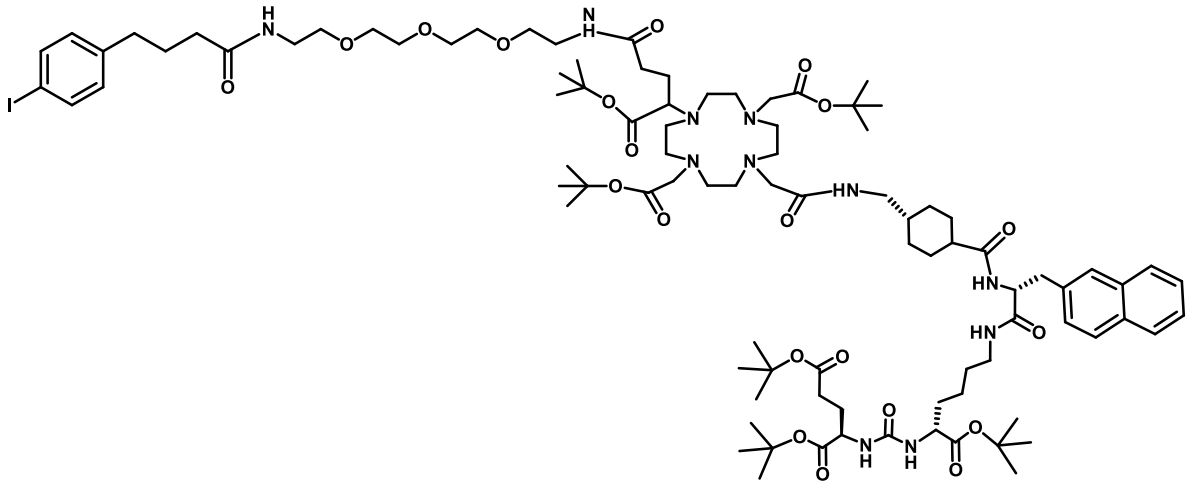

A solution of IPBA–PEG–DOTA–PSMA-(tBu)$_3$–COOH (6.7 mg, 0.00614 mmol), HBTU (3.7 mg, 0.00512 mmol), and DIPEA (3.5 µL, 0.0205 mmol) in dry DMF (1.2 mL) was stirred for 10 minutes at room temperature. Subsequently, PSMA–(tBu)$_3$ (4.22 mg, 0.00512 mmol) and

additional DMF were added to the reaction mixture. The solution was stirred for 2 hours, and the reaction progress was monitored by HPLC using Method A. After completion, the volatiles were removed under reduced pressure, and the resulting residue was purified using a Sep-Pak C18 cartridge. Elution was carried out with a mixture of 0.1% TFA in water and 0.1% TFA in ACN, with a stepwise increase in the organic phase percentage during elution. The fractions containing the desired product were combined and lyophilized to afford IPBA–PEG–DOTA–PSMA-$(tBu)_3$. ESI(+)-MS (*m/z*): $[M + 2H]^{2+}$ calcd: 949.01; found: 949.11.

2.3.7 Synthesis of IPBA–PEG-DOTA-PSMA: (((1R)-1-carboxy-5-((2R)-2-(4-((2-(7-(1-carboxy-21-(4-iodophenyl)-4,18-dioxo-8,11,14-trioxa-5,17-diazahenicosyl)-4,10-bis(carboxymethyl)-1,4,7,10-tetraazacyclododecan-1-yl)acetamido)methyl)cyclohexane-1-carboxamido)-3-(naphthalen-2-yl)propanamido)pentyl)carbamoyl)-D-glutamic acid

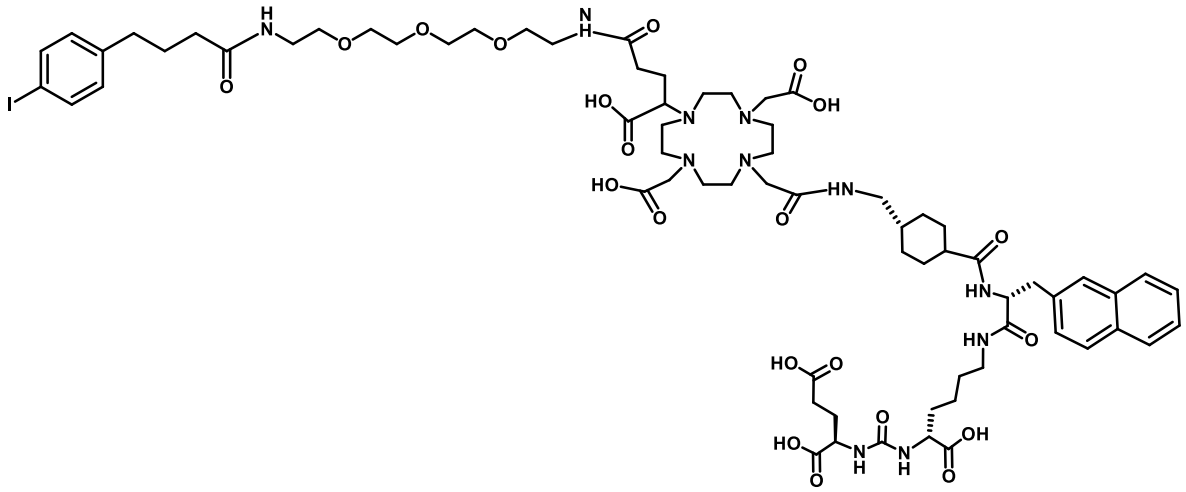

Compound IPBA–PEG–DOTA–PSMA-$(tBu)_3$ was dissolved in 2mL of a mixture of TFA and water that was stirred overnight at room temperature. After this time the reaction progress was monitored by HPLC using method C and then, the volatiles were removed under vacuum. The crude was redissolved in ACN and purified by HPLC using again Method C. The collected fractions were lyophilized to afford IPBA–PEG-DOTA-PSMA, as white powder (1.5 mg, 9.62e-7 mol, 16% of yield). ESI(+)-MS m/z calcd for $C_{70}H_{102}IN_{11}O_{21}$: $[M + H]^+$ calcd 1560.64, found 1560.76; $[M + 2H]^{2+}$ calcd 780.32, found 780.90.

2.4 Synthesis of Natural Indium

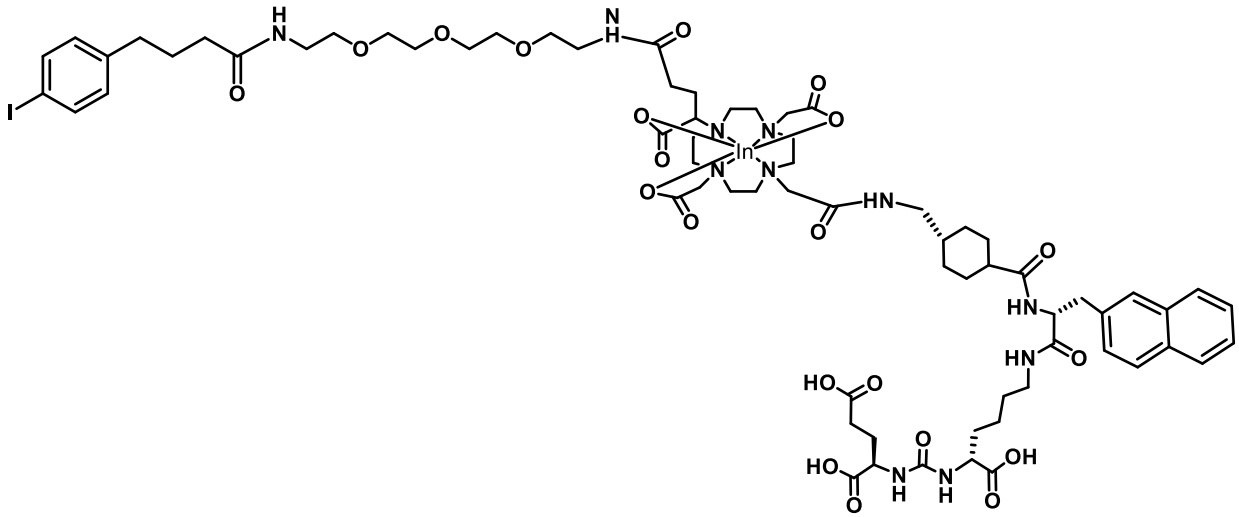

60 µL of IPBA–PEG–DOTA–PSMA solution (20 µL of ligand and 40 µL of 0.1 M sodium acetate buffer, (pH 5) were mixed with 6 µL of $InCl_3$. Sodium acetate buffer (0.1 M, pH 5) was added to reach a final reaction volume of 500 µL. The solution was heated to 95 °C for 30 min to allow complexation. The mixture was purified by Sep-Pak cartridges C-18 and the complex was eluted with 0.5 mL ACN 0.05% TFA. The reaction was quantitative. The complex was identified by HPLC and analysed by ESI-MS analysis. ESI(+)-MS: m/z calcd for $[M+H+K]^{2+}$: 855.403; found: 855.738.

2.5 Radiolabeling with ^{111}In

The radioconjugate [^{111}In]In–IPBA–PEG–DOTA–PSMA was prepared following a standard procedure commonly used for the radiolabeling of DOTA-based ligands with Indium-111. A 1.5 mg sample of IPBA–PEG–DOTA–PSMA (M = 1560.64 g·mol^{-1}) was dissolved in 200 µL of water and 300 µL of sodium acetate buffer (0.4 M, pH 5.0) to prepare a 1.924 mM stock solution. An aliquot of 20 µL of this stock was then diluted with 80 µL of 0.1 M sodium acetate buffer (pH 5.0) to obtain a 0.3848 mM working solution.
Radiolabeling reactions were carried out at different total volumes (125 µL, 250 µL, and 500 µL), maintaining the final ligand concentration constant at 10 µM.
A typical labeling reaction (total volume 125 µL) contained:

- 3.3 µL of the IPBA–PEG–DOTA–PSMA working solution (10 µM final concentration),
- 5 µL of $^{111}InCl_3$ (4.05 MBq, 0.01 M HCl)
- 116.7 µL of 0.1 M sodium acetate buffer (pH 5.0).

The reaction mixture was gently mixed and incubated at 95 °C for 15 min.
After incubation, the radiochemical yield (RCY) and radiochemical purity (RCP) of [^{111}In]In–IPBA–PEG–DOTA-PSMA were evaluated by radio-HPLC (γ-detection) and TLC.
The chromatogram displayed a single radioactive peak at 15.7 min corresponding to the desired radiocomplex, confirming the complete incorporation of ^{111}In into the DOTA chelator. All radiolabeled preparations exhibited RCYs higher than 95%.
The chemical identity of the radiolabeled complex was confirmed by co-injection with the corresponding non-radioactive In(III) complex under identical chromatographic conditions.

2.6 Radiochemical in vitro Stability

The in vitro stability of [^{111}In]In–IPBA–PEG–DOTA–PSMA was evaluated by radio HPLC. The test was performed in two different media: phosphate-buffered saline (PBS, 0.1 M, pH 7.4), which simulates physiological conditions, and RPMI 1640 cell culture medium, which mimics a biological environment rich in biomolecules. For each test, 20 µL of the radiocomplex solution were diluted with 40 µL of the selected medium. The samples were incubated at 37 °C, and aliquots were collected after 24 and 48 hours. Each aliquot was analyzed by radio HPLC to check the integrity of the radiocomplex over time.

2.7 Lipophilicity Determination

Lipophilicity is an important physicochemical property that can influence a compound's potency, pharmacokinetics and toxicity. It reflects how a molecule distributes between aqueous and lipid environments, affecting its ability to cross biological membranes. The most common way to measure lipophilicity is through the shake-flask method, which determines the distribution of a compound between 1-octanol and an aqueous buffer. The obtained value, expressed as log $D_{pH7.4}$, provides a practical indication of lipophilicity and is still considered the reference method [52].
The lipophilicity of [^{111}In]In–IPBA–PEG–DOTA-PSMA was determined using the classical shake-flask method. An aliquot of 20 µL of the radiolabelled compound (typically 1–5 MBq) was added to a mixture of n-octanol (0.5 mL) and PBS (0.5 mL, pH 7.4), previously saturated with each other by stirring. The mixture was vortexed and centrifuged at 3000 rpm for 10 minutes at room temperature to allow phase separation. After separation, samples from both the octanol and aqueous phases were transferred into four Eppendorf tubes each, and the radioactivity was measured in a gamma counter. The mean activity in each phase was used to calculate the distribution coefficient (D), as the ratio between the activity in the octanol and aqueous phases. The results were expressed as log $D_{pH7.4}$.

2.8 Cellular studies

2.8.1 Cell culture

The PC3 PIP ($PSMA^+$) and PC3 Flu ($PSMA^-$) human prostate cancer cell lines were kindly provided by Prof. Dr. Martin Pomper (Johns Hopkins University School of Medicine, Baltimore, MD, USA). Cells were cultured in RPMI-1640 medium supplemented with 10% fetal bovine serum (FBS) and 1% penicillin/streptomycin. To maintain PSMA expression in the $PSMA^+$ PC3 PIP cells, the culture medium was further supplemented with 0.02% puromycin. All cell culture reagents were purchased from Gibco (Thermo Fisher Scientific, Waltham, MA, USA). Cell cultures were maintained in a humidified incubator at 37 °C under a 5% CO_2 atmosphere, and were routinely tested for mycoplasma contamination using the LookOut Mycoplasma PCR Detection Kit (Sigma-Aldrich).

2.8.2 Cellular uptake, internalization and blocking

The cellular uptake and internalization of [^{111}In]In–IPBA–PSMA–PEG–DOTA were investigated in PSMA-positive (PC3 PIP) and PSMA-negative (PC3 Flu) prostate cancer cell lines to assess PSMA-mediated binding and internalization (figure 2.16).

Cells were seeded in 24-well plates at a density of 1.5×10^5 cells per well and allowed to attach overnight at 37 °C in a humidified atmosphere containing 5% CO_2. A fresh solution of [^{111}In]In–IPBA–PSMA–PEG–DOTA (≈ 6.66 µCi in 20 mL) was prepared in RPMI-1640 medium supplemented with 10% fetal bovine serum (FBS) and 1% penicillin/streptomycin. For blocking studies, 2-(phosphonomethyl)pentanedioic acid (2-PMPA) was prepared in the same medium at a final concentration of 200 µM (from a 10 mM stock; 70 µL stock + 3.43 mL medium).
Before incubation, the culture medium was aspirated from the wells. For blocking conditions, 250 µL of the 2-PMPA solution were added and cells were pre-incubated for 30 min at 37 °C. For uptake and internalization assays, 250 µL of supplemented medium were added. Subsequently, 250 µL of the radiocomplex solution were added to all wells, resulting in a final volume of 0.5 mL per well. In parallel, 250 µL of the same radiocomplex solution were dispensed into RIA tubes to determine the total added radioactivity.
Cells were incubated for 5, 30, 60, 120, 180, and 240 min at 37 °C. At each time point, the supernatant containing unbound activity was removed and cells were washed with 0.5 mL of ice-cold RPMI medium (without supplements). The surface-bound activity was removed by two consecutive washes with 0.5 mL of 50 mM glycine-HCl / 100 mM NaCl buffer (pH 2.8) for 4 min at room temperature. The acid washes were combined in the same RIA tube, followed by a brief PBS rinse to neutralize the pH, which was also collected in the same tube.
Cells were then lysed with 0.5 mL of 1 M NaOH for at least 10 min at 37 °C to quantify internalized activity. The lysates were collected in separate RIA tubes and the radioactivity of both surface bound and internalized fractions was measured using a gamma counter. Total cellular uptake was calculated as the sum of both fractions and expressed as a percentage of the total added radioactivity per well. Each time point was performed in quadruplicate and results were expressed as the percentage of total activity added to the cells.

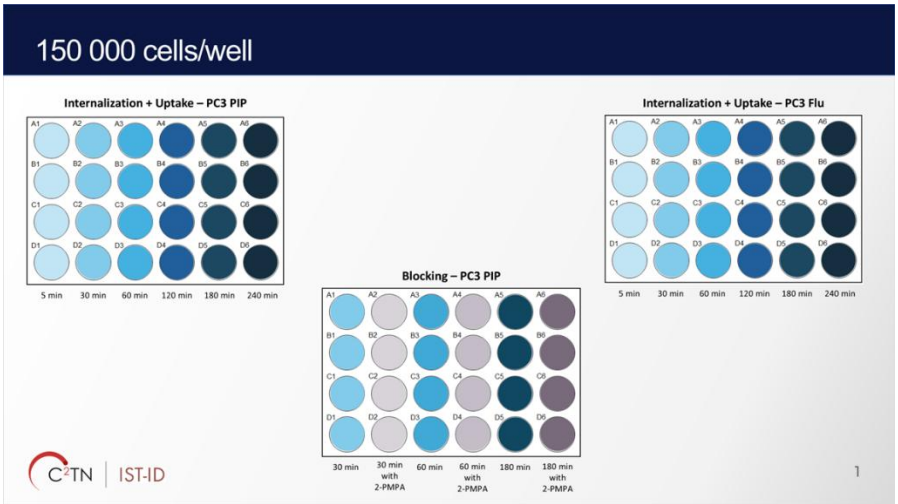

Figure 2.16: Internalization, uptake and blocking studies of [^{111}In]In–IPBA–PSMA–PEG–DOTA in PC3 PIP and PC3 Flu cells.

2.9 In vivo biodistribution studies

The in vivo biodistribution of [^{111}In]In–IPBA–PSMA–PEG–DOTA was evaluated in groups of three female CD-1 mice (randomly bred, Charles River) weighing approximately 25 g each. As shown in figure 2.17 the animals were intravenously injected via the tail vein, with 100 µL of the radiocomplex, corresponding to an activity of 4.2–5.3 MBq, and were maintained on a normal diet ad libitum. All experiments were performed in compliance with the highest standards of animal care and according to European legislation.

Figure 2.17: Administration of the radiotracer by tail-vein injection in mice. Adapted from [53].

Mice were sacrificed by cervical dislocation at 1, 2, 4, and 24 hours post-injection. The injected dose and the residual activity in the carcass after sacrifice were measured using a dose calibrator.
The difference between these values was assumed to correspond to the total excreted activity. Blood samples were collected by cardiac puncture at the time of sacrifice. Major organs and tissues were dissected, weighed, and the associated radioactivity was measured using a γ-counter (HIDEX AMG, Hidex, Turku, Finland). The biodistribution results were expressed as the percentage of injected activity per gram of tissue %IA/g according to the following formula:

$$\%IA/g = \left(\frac{Activity\ in\ organ\ (Bq)}{Injected\ acrivity\ (Bq) \times Organ\ mass(g)}\right) \times 100 \qquad (2.17)$$

This value represents the fraction in percent of the total injected activity that is localized in one gram of a specific tissue.
Blood samples were centrifuged to separate the serum, which was treated with ethanol to precipitate proteins. The supernatant, as well as urine samples (centrifuged at 3000 rpm for 10 min), were analyzed by radio-HPLC to assess the in vivo stability of the radiocomplex**.**

2.10 µSPECT/CT Imaging

SPECT/CT acquisitions were performed using a FLEX® Triumph® II (Trifoil Imaging) preclinical imaging system (figure 2.18) equipped with a Cadmium Zinc Telluride (CZT) detector and a five-pinhole (1.0 mm) collimator (N5F75A10). SPECT data were acquired for 30 s per projection, with a stepwise rotation of 128 projections over 360°, accounting for the decay of Indium-111.

Figure 2.18: FLEX® Triumph® II preclinical imaging system (Gamma Medica) used for µSPECT/CT acquisitions.

Cone-beam CT images were acquired in gantry step-motion mode (512 projections, 165 ms per projection, 40 kVp, 740 µA) with 2×2 binning and an image matrix of 1184 × 1120 pixels. Reconstruction of SPECT images was carried out using the Triumph Reconstruction Application v1.0.8.0 (Trifoil Inc.), employing a 3D-ordered subset expectation maximization (3D-OSEM) algorithm with 8 subsets and 5 iterations to obtain transaxial, coronal, and sagittal slices.
Post-processing analysis and coregistration of SPECT and CT images were performed using Vivid Amira 4.1 software (Thermo Fisher Scientific). A Gaussian filter ($\sigma = 0.6$, 3×3 kernel) was applied to the CT slices with a threshold value of 1750.

2.11 Serum Protein Binding Assay (Zeba Spin Method)

A comparative study was performed to evaluate the interaction of [^{111}In]In–IPBA–PEG–DOTA-PSMA, which contains an albumin-binding domain and [^{111}In]In–PSMA presents in [51], which lacks this moiety. The aim was to assess the effect of the albumin-binding domain on serum protein affinity.
Protein binding was evaluated using Zeba Spin desalting columns (7 kDa molecular weight cut-off, Thermo Fisher Scientific). This method enables the separation of high-molecular-weight proteins, such as albumin, which are eluted in the filtrate, from unbound low molecular weight compounds that remain within the resin.
For each experiment, 100 µL of the radiolabeled compound were incubated with an appropriate volume of human serum at room temperature per 30 minutes. The mixtures were then loaded onto pre-equilibrated Zeba Spin columns and centrifuged for 2 min at 1500 rcf to separate the protein bound and unbound fractions.
Control samples containing only [^{111}In]In–IPBA–PEG–DOTA-PSMA or [^{111}In]In–PSMA (without serum) were processed under the same conditions to assess non specific binding to the

resin.
Radioactivity in the total and eluted fractions was measured with a gamma counter, and the percentage of protein bound fraction was calculated as the ratio between the activity in the filtrate (protein bound) and the total activity.

Chapter 3

Results and Discussion

3.1 Chemical Synthesis and Characterization of the Conjugates

3.1.1 Protected PSMA-Binding Domain Synthesis

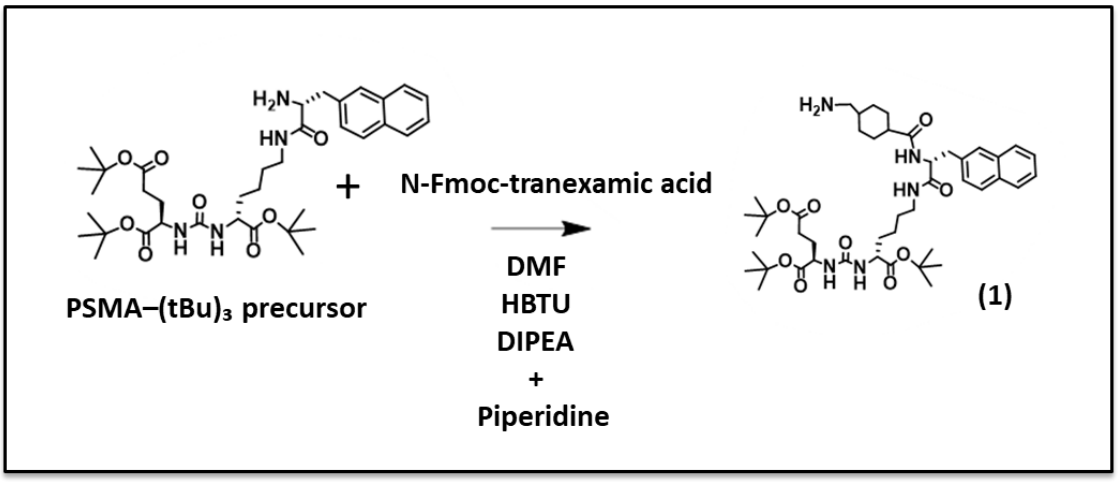

Figure 3.19: Synthesis of protected PSMA–Binding Domain (1).

Figure 3.19 provides an overview of the synthesis of the PSMA-binding unit. The starting material was the tBu-protected PSMA precursor (PSMA–$(tBu)_3$), previously prepared in our laboratory following the procedure reported by Santos et al. [51]. This precursor already contains the PSMA-recognition motif and offers a free amine that can be further functionalised. Synthesis of Compound 1 follows a two step sequence. In the first step, the free amine of the PSMA precursor was coupled with commercially available N-Fmoc-tranexamic acid, whose amine is protected with an Fmoc group, giving the corresponding Fmoc-protected intermediate. In the second step, the Fmoc protecting group on the tranexamic amine was removed using piperidine, yielding the final PSMA-binding fragment, identified as Compound 1.

Analytical HPLC showed a well-defined peak corresponding to the desired product, and ESI-MS confirmed the expected molecular ion (m/z calcd for $[M+H]^+$: 824.51; found: 824.7 $[M+H]^+$), supporting the successful formation of the amide bond.

This transformation represents a key stage in assembling the PSMA-binding domain. The amide linkage provides high chemical stability, while the tranexamic acid fragment contributes rigidity and proper spatial orientation for efficient PSMA recognition. Overall, the formation of Compound 1 completes the structural features required for selective interaction with the PSMA receptor and establishes the basis for the construction of the heterobivalent conjugate.

3.1.2 Albumin-binding domain synthesis

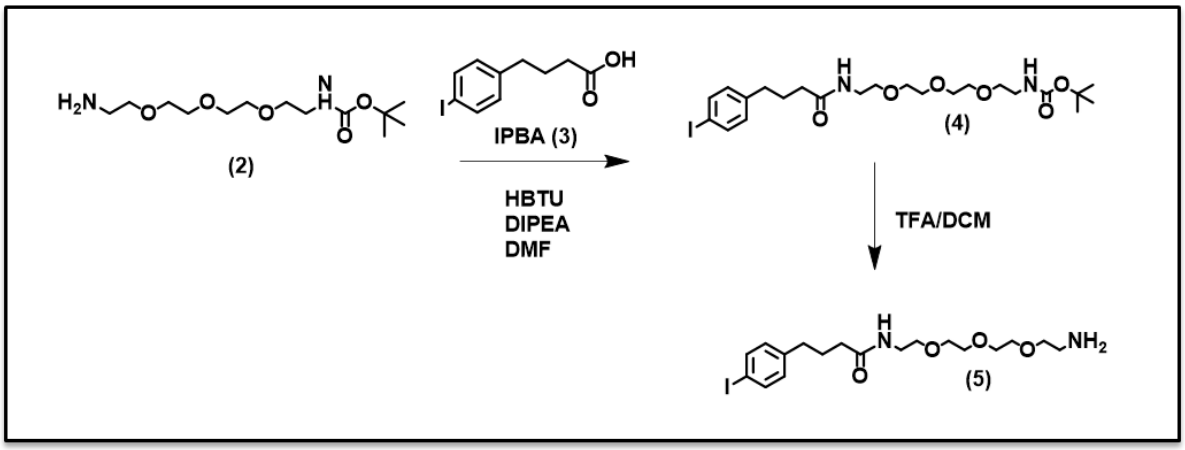

Figure 3.20: Synthesis of albumin-binding moiety IPBA–PEG–NH_2 (5).

The albumin-binding domain was introduced through the conjugation of IPBA a wellestablished small molecule known to enhance the pharmacokinetic properties of PSMA-targeted radiopharmaceuticals. The coupling between IPBA and the Boc-protected PEG linker (figure 3.20) was achieved under mild conditions using HBTU and DIPEA as activating and coupling agents, leading to the formation of a stable amide bond. After purification and Boc deprotection, the expected product was obtained, as confirmed by HPLC analysis showing a retention time of 15.2 minutes (figure 3.21). Figure 3.23 shows the ESI(+)-MS analysis, confirming the presence of the expected molecular ion and the successful formation of the compound.

The IPBA moiety contains an aromatic iodophenyl group, which interacts reversibly with serum albumin through hydrophobic contacts. These interactions occur between the non polar aromatic ring of IPBA and hydrophobic regions of the protein, allowing a transient, non-covalent association. This reversible binding helps extend the circulation time of the compound in blood while maintaining its ability to reach PSMA-expressing tissues.

The inclusion of IPBA as an albumin-binding moiety provides a balanced interaction strong enough to prolong systemic exposure, yet reversible enough to ensure efficient tumor delivery. In this way, IPBA contributes to improve pharmacokinetic performance and enhance tumor targeting efficiency of the final radioconjugate [27].

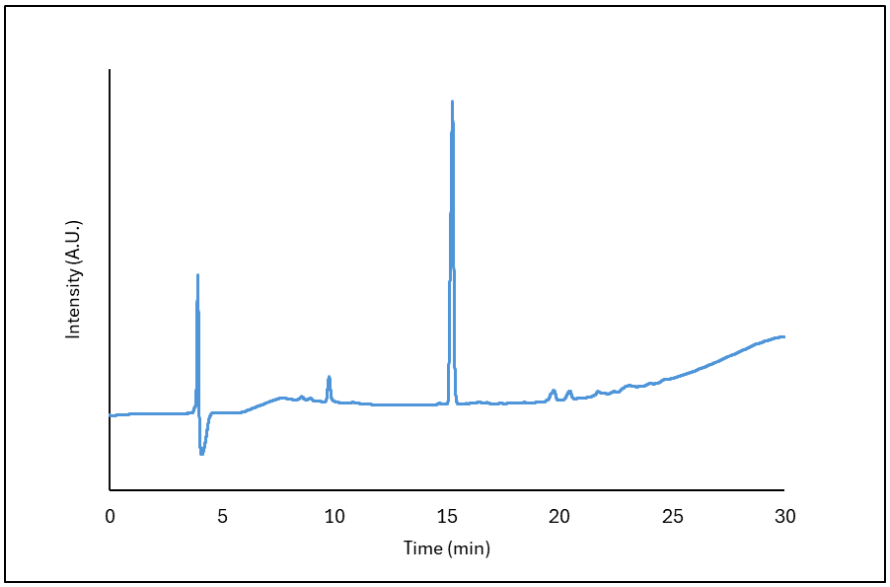

Figure 3.21: HPLC chromatogram of the albumin-binding moiety IPBA–PEG–NH_2 (Method A, Rt=15.2, 220 nm).

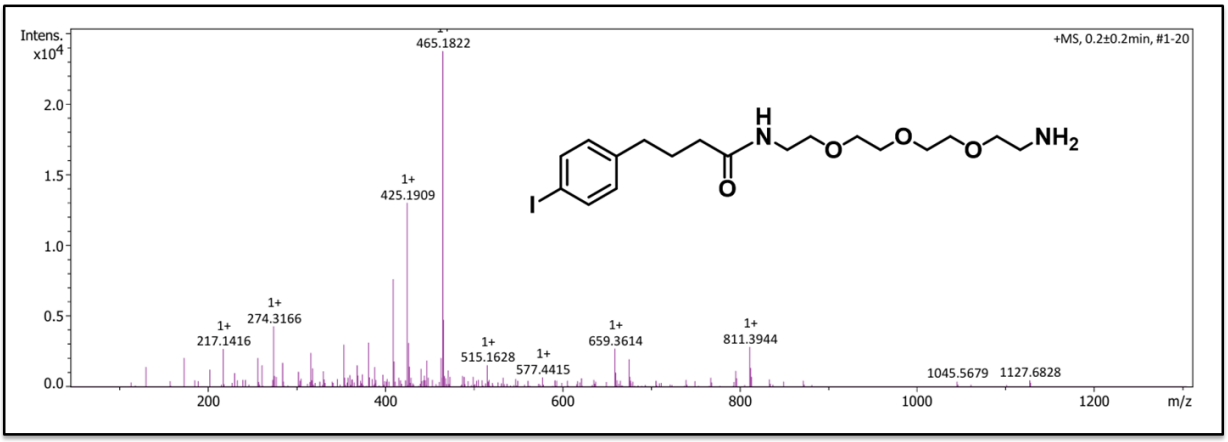

Figure 3.22: ESI–MS spectrum of the conjugate IPBA–PEG (5) in the positive ion mode (m/z calculated for $[M+H]^+$ 465.12; found 465.18) and representation of its chemical structure (molecular formula $C_{18}H_{29}IN_2O_4$; molecular weight 464.34 Da).

3.1.3 Conjugation of the Albumin-Binding Domain to the DOTA-Based Prochelator

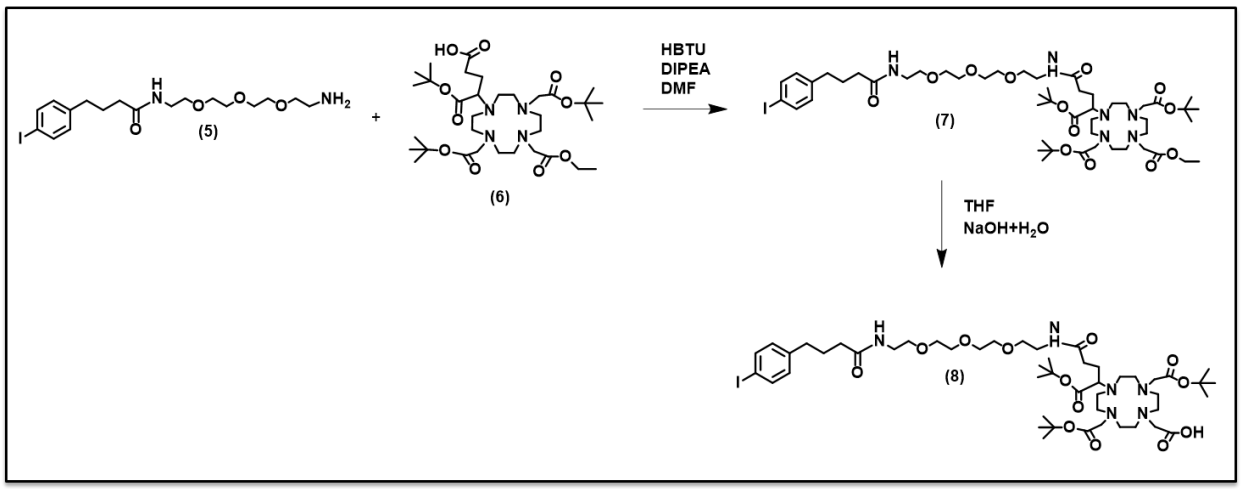

Figure 3.23: Synthesis of the DOTA-Based Prochelator IPBA–PEG–DOTA-(tBu)$_3$–COOH.

The synthesis of IPBA–PEG–DOTA-(tBu)$_3$–COOH was performed according to the scheme presented in figure 3.23. The conjugation of the albumin-binding fragment IPBA to the DOTA monoethyl ester derivative (compound 6) was achieved through an amide coupling reaction using HBTU and DIPEA in dry DMF at room temperature.

The formation of the intermediate IPBA–PEG–DOTA-(tBu)$_3$–Et (7) was monitored by analytical HPLC and confirmed by ESI(+)-MS analysis. After 24 hours of stirring, the volatiles were removed and the crude product was purified by silica gel column chromatography using DCM and MeOH as eluents. The product was obtained as a yellow oil. The ESI(+)-MS spectrum confirmed the formation of the expected product, demonstrating the successful coupling between the DOTA and IPBA units through the PEG linker. The selective hydrolysis of the ethyl ester group in compound 7 was carried out under basic conditions using NaOH in a mixture of THF and water. The reaction mixture was stirred overnight at room temperature, and its progress was monitored by HPLC. After completion, the crude was neutralized with HCl and extracted into CFM. The organic phase was dried and purified by semi-preparative HPLC using method B. The obtained compound, IPBA–PEG–DOTA-(tBu)$_3$–COOH (8), was isolated as a yellow oil. Figure 3.24 presents the ESI(+)-MS analysis, confirming the expected molecular ion pattern consistent with the formation of the desired compound.

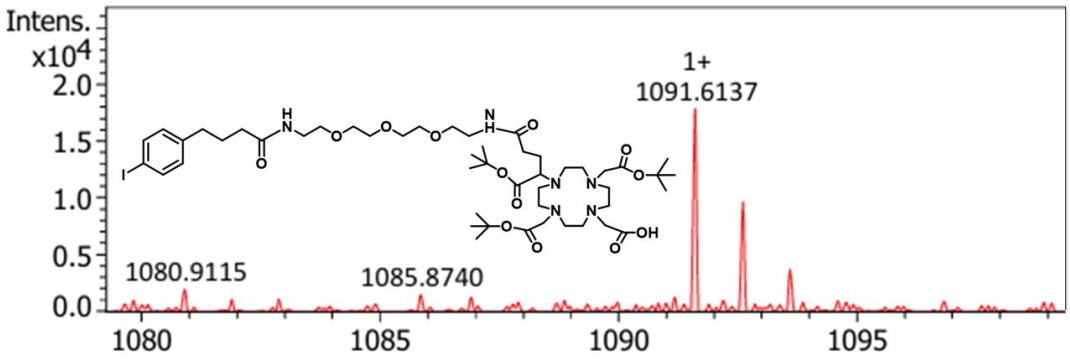

Figure 3.24: ESI–MS spectrum of the conjugate IPBA–PEG–DOTA-(tBu)$_3$–COOH (8) in the positive ion mode (m/z calculated for $[M+H]^+$ 1091.51; found 1091.61) and representation of its chemical structure (molecular formula $C_{48}H_{74}IN_6O_{12}$; molecular weight 1091.41 Da).

3.1.4 Synthesis of the Heterobivalent Conjugate IPBA–PEG–DOTA–PSMA

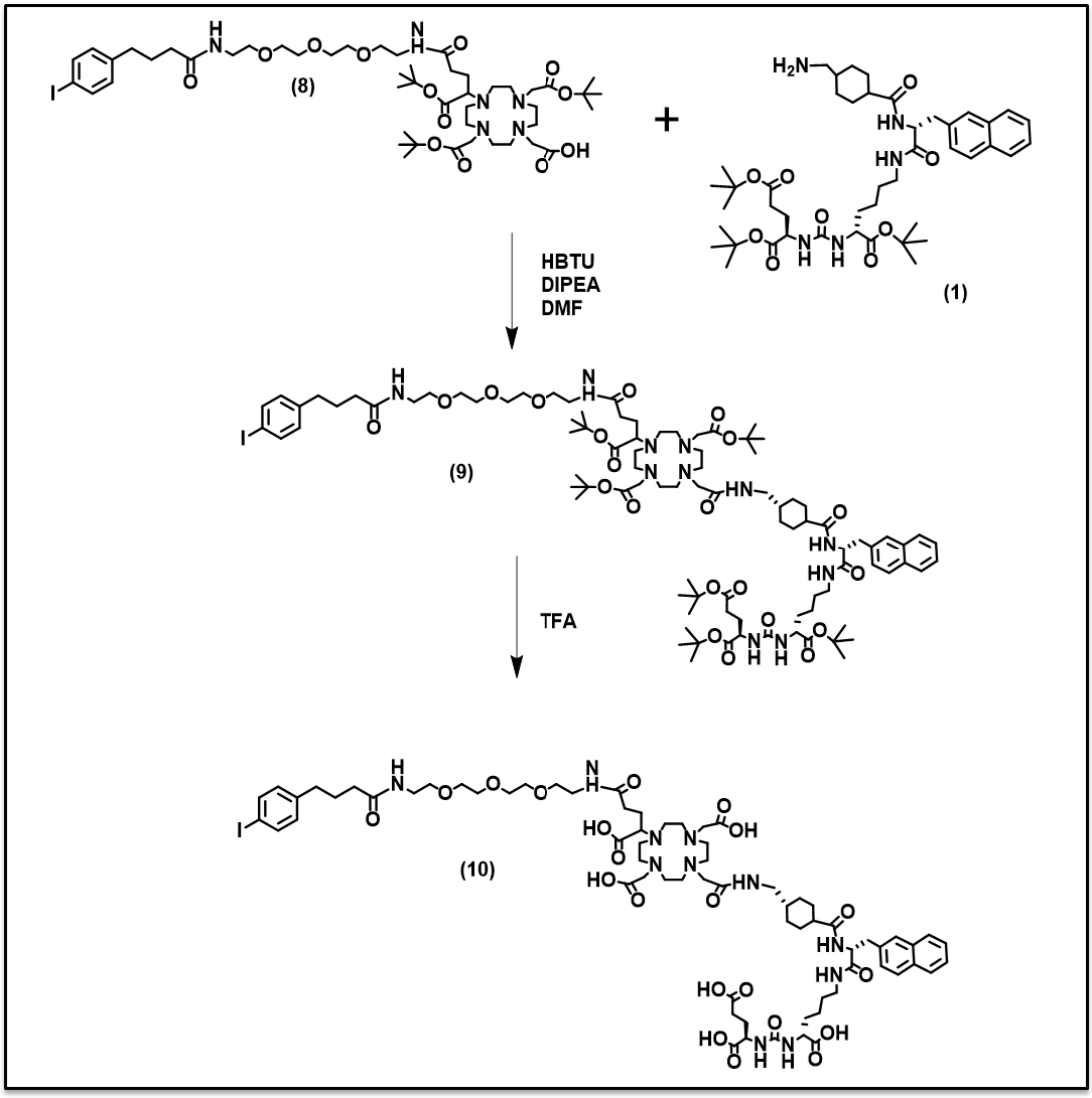

Figure 3.25: Synthesis the Heterobivalent Conjugate IPBA–PSMA–PEG–DOTA.

Figure 3.25 presents the synthesis of the final conjugate, achieved in two steps, starting from compound 8. In the first step, the DOTA-based intermediate was coupled with the PSMA-targeting unit using HBTU as the coupling reagent and DIPEA as a base, in dry DMF at room temperature. The reaction was stirred for 2 hours and its progress was followed by HPLC. After completion, the crude product was purified using a Sep-Pak C18 cartridge and eluted with a gradient of ACN containing 0.1% TFA. The collected fractions were combined and lyophilized to obtain compound 9 as a yellow solid.

In the second step, the tert-butyl protecting groups of compound 9 were removed using TFA. The reaction was carried out overnight at room temperature, and its progress was checked by HPLC. Figure 3.26 shows the chromatogram of IPBA–PEG–DOTA–PSMA, which displays a retention time of 10.2 minutes. After evaporation of the solvent and purification by HPLC, the final product 10 was obtained as a white powder.

Figure 3.27 shows the ESI(+)-MS analysis of the deprotected conjugate, confirming the complete removal of the tBu protecting groups and the successful formation of the free DOTA chelating unit.

These two step synthesis successfully, led to the formation of the heterobivalent conjugate combining both the PSMA-targeting and albumin-binding domains. The final compound contains a deprotected DOTA group. The deprotection of the DOTA group is important because it makes the chelator active and ready to bind metal ions such as Indium or Lutetium. This step is essential to allow the final compound to be radiolabeled and used in imaging or therapy applications.

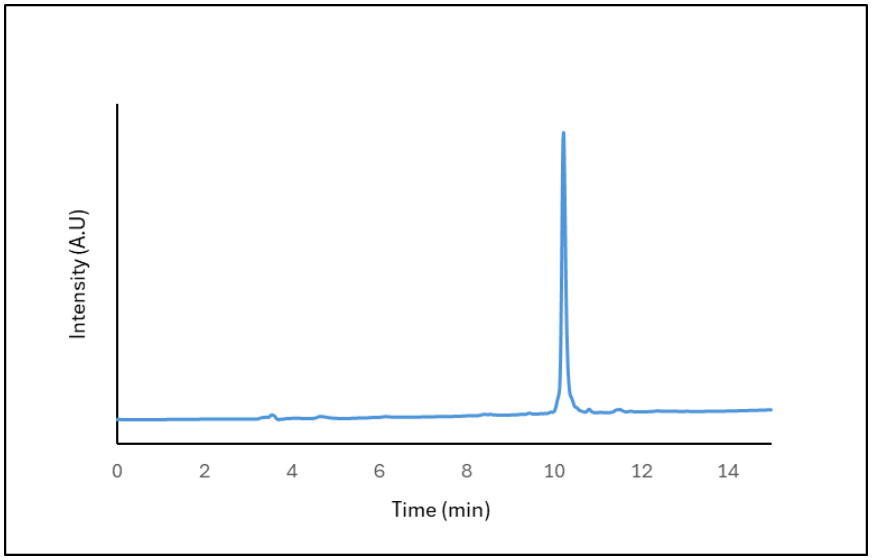

Figure 3.26: HPLC chromatogram of IPBA–PEG–DOTA–PSMA (Method C, Rt = 10.2 min, 220 nm).

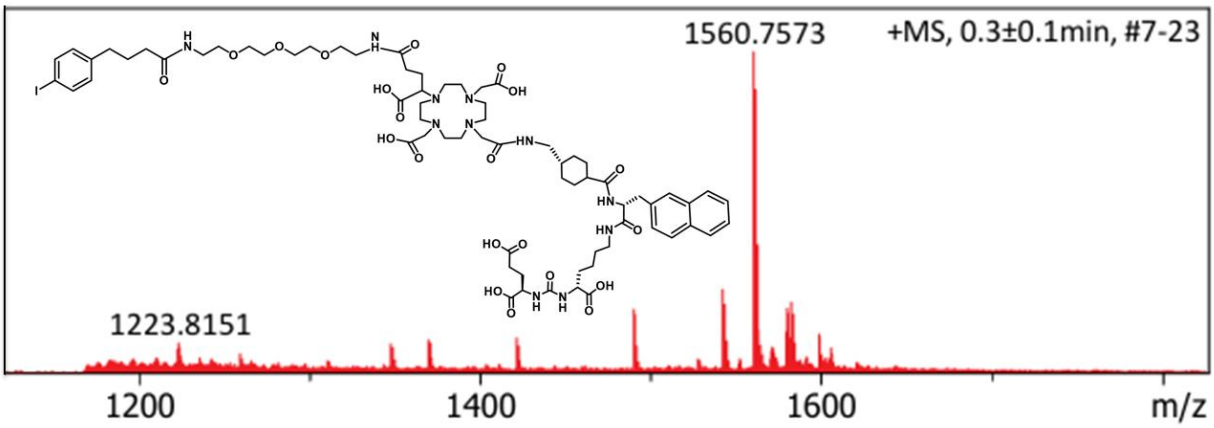

Figure 3.27: ESI(+)-MS spectrum of the final conjugate IPBA–PEG–DOTA–PSMA (10) in the positive ion mode, showing the $[M+H]^+$ molecular ion (m/z calcd 1560.63; found 1560.76), together with the representation of its chemical structure (molecular formula $C_{70}H_{103}IN_{11}O_{20}$; molecular weight 1560.55 Da).

3.2 Synthesis and Characterization of the Natural Indium Complexes

The characterization of radiolabelled compounds is generally quite challenging, since their mass is usually negligible and the standard analytical techniques, such as Nuclear Magnetic Resonance (NMR) or ESI-MS, are not sensitive enough to detect them. Therefore, for the chemical characterization of new radiolabelled compounds, the corresponding non-radioactive complexes are prepared as surrogates of the radioactive ones, taking advantage of their identical chemical structure.

This approach allows, not only to determine the physico-chemical properties of new potential radiopharmaceuticals, but also to confirm their chemical identity. Generally, the complexes are analyzed by HPLC together with their corresponding radiocomplexes and, their chromatographic profiles and retention times are expected to be identical. To obtain the Indium complex necessary to identify the [^{111}In]In–IPBA–PEG–DOTA–PSMA radiocomplex, the complexation of the ligand IPBA–PEG–DOTA–PSMA with the In(III) was carried out using natural Indium.

Taking into consideration the coordination behaviour and solution chemistry of the In(III) metal ion, the reaction was performed in sodium acetate buffer (0.1 M, pH 5) by heating at 95 °C for 30 min. The formation of the desired [natIn]In–IPBA–PEG–DOTA–PSMA complex was quantitative. The purification to remove the excess of Indium ions was achieved using Sep-Pak C18 cartridges, and the complex was eluted with ACN containing 0.05 % TFA.

After purification, the product was analysed by HPLC and ESI-MS. In figure 3.28, HPLC analysis reveals a single peak corresponding to the Indium complex, with a retention time of 15.3 min. Figure 3.29, instead shows ESI-MS spectrum that confirms the expected molecular mass, validating the successful formation and identity of the natIn-labelled compound.

This experimental profile confirms the successful coordination of In(III) to the IPBA–PEG–DOTA–PSMA ligand and validates the identity of the natIn-labelled complex.

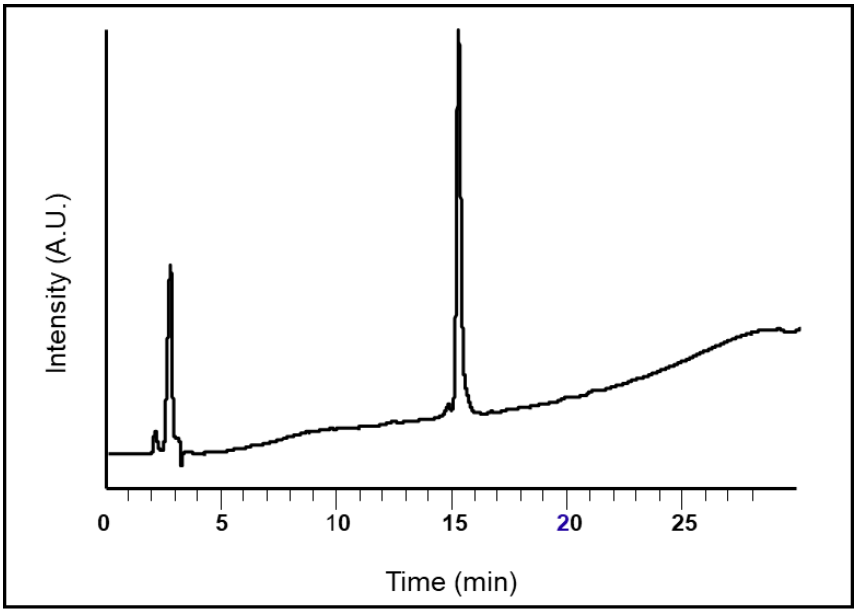

Figure 3.28: HPLC chromatogram of [natIn]In–IPBA–PEG–DOTA–PSMA (Method D, Rt = 15.3 min, 254 nm).

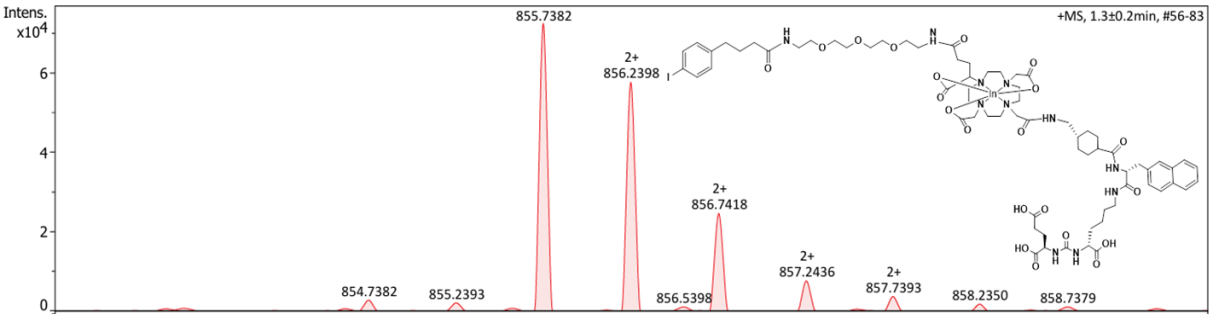

Figure 3.29: ESI–MS spectrum of the [natIn]In–IPBA–PEG–DOTA–PSMA complex in the positive ion mode (m/z calculated for $[M+H+K]^{2+}$ 855.403; found 855.738) together with the representation of its chemical structure (molecular formula $C_{70}H_{99}IInN_{11}O_{21}$, molecular weight 1672.32 Da).

3.3 Radiosynthesis and Characterization of ^{111}In-Radioconjugates

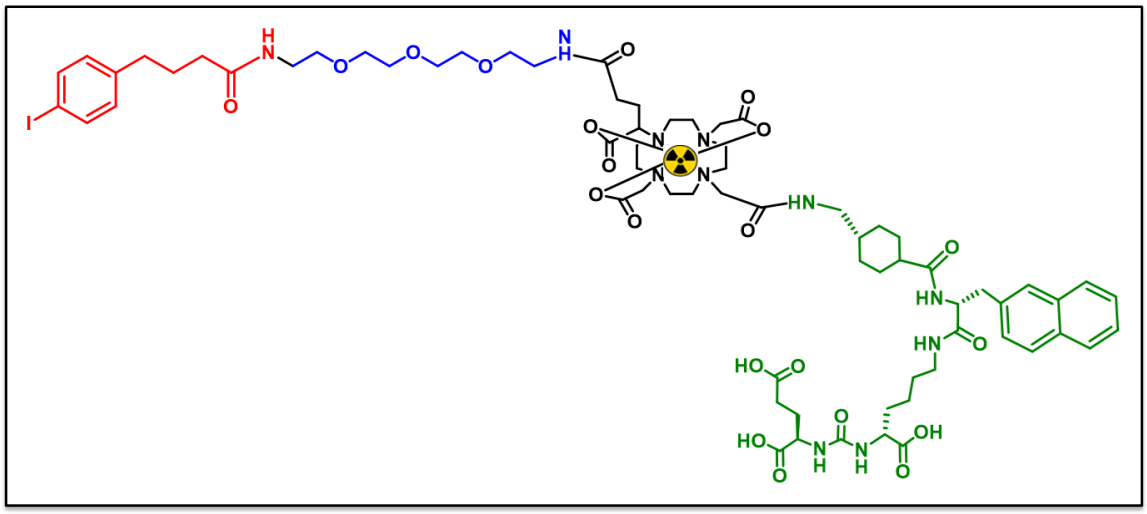

Figure 3.30: Chemical structure of the [^{111}In]In-IPBA-PEG-DOTA-PSMA radioconjugate, including the PSMA-targeting motif (green), PEG linker (blue), albumin-binding moiety IPBA (red), and DOTA chelator (black) complexed with Indium-111.

The radiolabelling of IPBA–PEG–DOTA–PSMA with Indium-111 was carried out under the standard conditions commonly used for DOTA-based chelators, as illustrated in figure 3.30. The ligand was dissolved in 0.4 M sodium acetate buffer (pH 5.0) to reach a final concentration of about 10 µM, and an aliquot of $^{111}InCl_3$ was added. The reaction mixture was then heated at 95 °C for 15 minutes to allow complete complexation.
The radiochemical purity (RCP) of the resulting [^{111}In]In–IPBA-PEG-DOTA-PSMA complex was analysed by HPLC equipped with a γ-detector. The chromatogram (figure 3.31) shows a single, sharp radioactive peak at a retention time of 15.7 minutes, indicating that only one radiochemical species was formed and that no unbound Indium-111 or degradation products are present.

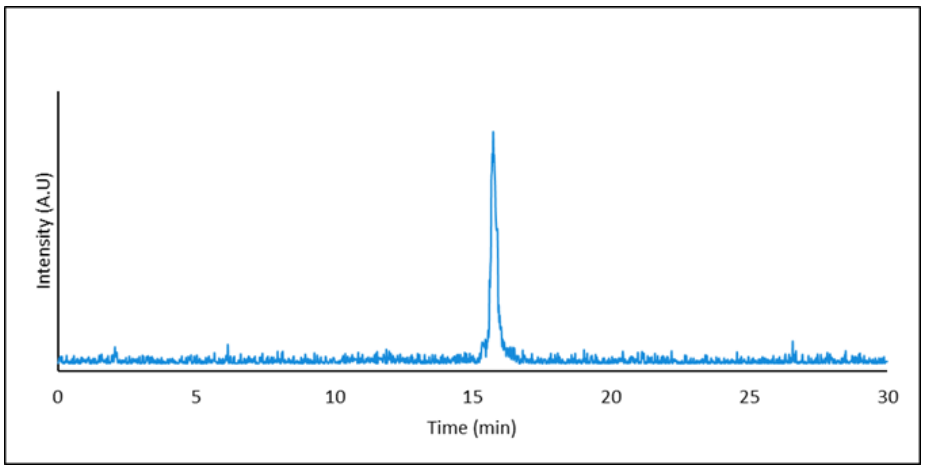

Figure 3.31: Radio-HPLC chromatogram of [^{111}In]In–IPBA–PEG–DOTA–PSMA (Method D, Rt = 15.7 min, γ-detection).

In order to confirm the identity of the radiolabelled compound, the non-radioactive Indium complex was co-injected together with the radiocomplex. Figure 3.32 shows the comparison

between the UV-chromatogram of the [natIn]In–IPBA–PEG–DOTA–PSMA complex and the γ-chromatogram of the corresponding [^{111}In]In–IPBA–PEG–DOTA–PSMA conjugate. The two traces display an almost perfect overlap of the main peak, with retention times of 15.3 min for the natIn complex and 15.7 min for the radiocomplex.
This close match confirms that both species share the same chemical identity and demonstrates that the labelling procedure successfully produced the desired Indium-111 complex. The same protocol was subsequently used for all radiolabelling steps carried out for *in vitro* and *in vivo* studies, ensuring consistency throughout the biological evaluation.

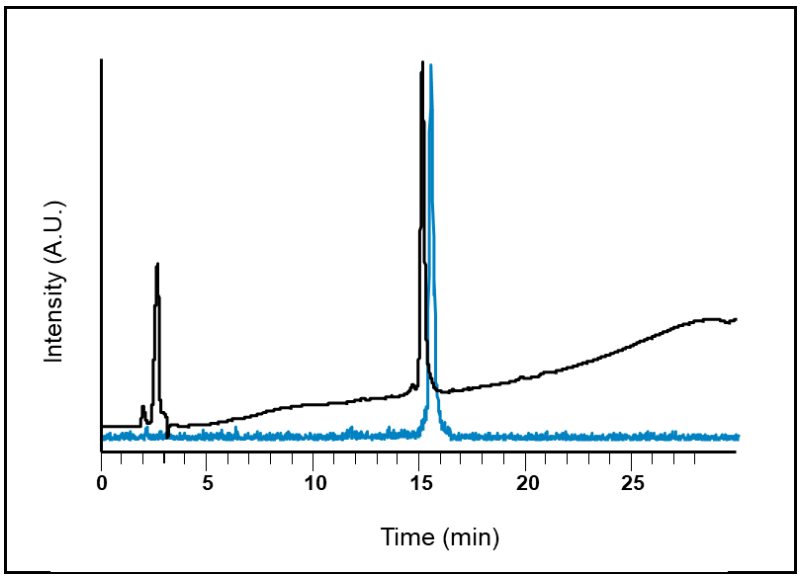

Figure 3.32: HPLC/γ-chromatograms comparison between the non-radioactive [natIn]In–IPBA–PEG–DOTA–PSMA complex (UV trace, Rt = 15.3 min) and the corresponding radiolabelled species [^{111}In]In–IPBA–PEG–DOTA–PSMA (γ-trace, Rt = 15.7 min), analysed under Method D (254 nm, γ-detection).

3.4 In vitro Evaluation Studies

The *in vitro* stability studies were carried out to confirm that the radiocomplex remained intact under the conditions used for the biological experiments. The test was performed in two different media: phosphate-buffered saline (PBS, 0.1 M, pH 7.4), a simple isotonic salt solution that mimics physiological conditions and RPMI-1640 cell culture medium, a nutrient-rich solution containing amino acids, vitamins, and glucose that reproduces the chemical environment typically found in cell cultures. [^{111}In]In-IPBA-PEG-DOTA-PSMA was incubated at 37 °C in both media for 24 and 48 hours, and the samples were analysed by HPLC at each time point. As shown in figure 3.33, the radiocomplex remained highly stable, showing a single sharp radioactive peak with no detectable degradation or free Indium-111 even after 48 hours. The retention time remained constant at around 15.7 minutes, confirming that the complex maintained its chemical integrity during incubation. These results demonstrate that [^{111}In]In–IPBA–PEG–DOTA–PSMA is stable under the same conditions used for the biological studies, ensuring the reliability of the cellular and biodistribution experiments.

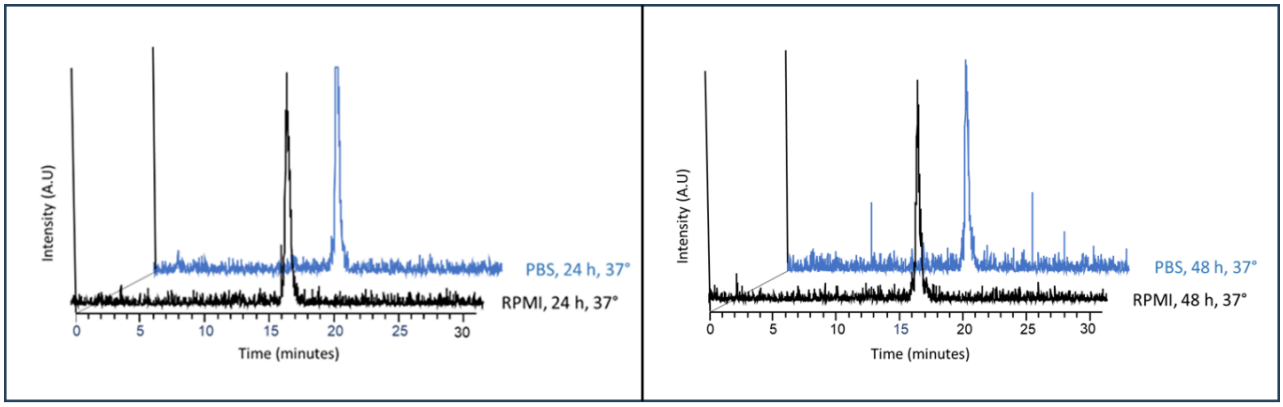

Figure 3.33: Radio-HPLC chromatograms of [^{111}In]In–IPBA-PEG-DOTA-PSMA after incubation in PBS (blue) and RPMI medium (black) at 37 °C for 24 h (left) and 48 h (right). The single peak at 15.7 min confirms the radiochemical stability of the complex in both media.

3.4.1 Lypophilicity determination

Lipophilicity plays a key role in determining the biodistribution and pharmacokinetic profile of radiopharmaceuticals. It reflects the balance between hydrophilic and lipophilic forces that influence how a compound crosses biological membranes and interacts with its molecular targets [55]. The lipophilicity of [^{111}In]In-IPBA-PEG-DOTA-PSMA was measured using the shake-flask method, comparing its distribution between n-octanol and water. The obtained log $D_{pH7.4}$, value of '–2.23' shows that the compound is highly hydrophilic. This result is consistent with its structure, which includes several polar components such as the DOTA chelator, the PEG linker, and the PSMA-binding unit.

Although the overall character is clearly hydrophilic, the molecule also contains the IPBA group, which can interact reversibly with serum albumin and therefore prolong its circulation time in blood, partially compensating for its low lipophilicity. This high hydrophilicity suggests that the radiocomplex is highly soluble in aqueous environments but has limited ability to passively cross lipid membranes. This is actually beneficial for PSMA-targeted compounds, as their uptake relies on specific receptor binding rather than non-selective diffusion across cell membranes. Such behaviour supports rapid renal clearance together with specific receptor-mediated uptake, while the albumin-binding IPBA unit contributes to a more favourable pharmacokinetic balance.

3.4.2 Albumin binding zeba spin

The incubation of the radiocomplexes with human serum showed a clear difference in their ability to bind to serum proteins.
For [^{111}In]In–IPBA–PEG–DOTA–PSMA, the total activity loaded onto the column was 1.67 MBq. After separation, 1.47 MBq of the activity was found in the protein bound fraction, while 0.20 MBq remained in the column. This corresponds to a protein binding of 88.2%, indicating a strong interaction with serum proteins.
In contrast, [^{111}In]In–PSMA showed a lower binding affinity. Out of a total of 2.47 MBq applied, 1.75 MBq were detected in the protein bound fraction and 0.73 MBq remained unbound, resulting in 71% protein binding.
Control experiments performed without serum, confirmed that both radiocomplexes were mostly retained by the column resin when no proteins were present. Under these conditions, only 11% of the activity for [^{111}In]In–IPBA–PEG–DOTA–PSMA and 20% for [^{111}In]In–PSMA were eluted. This confirmed that the amout of activity measured in the filtrate originated from protein binding interactions, and was not influenced by the column separation process.
Overall, the higher binding, observed for [^{111}In]In–IPBA–PEG–DOTA–PSMA, confirms the expected role of the IPBA moiety as an albumin-binding group. This stronger interaction with serum proteins is likely to prolong the circulation time of the radioconjugate in vivo, which could enhance its tumor uptake and retention, compared to the [^{111}In]In–PSMA analogue that lacks this domain.

3.4.3 Cellular uptake, internalization and blocking studies

The cellular studies were performed using the prostate cancer cell lines PC3-PIP and PC3-FLU. Both originate from the same parental PC3 line, which is PSMA-negative and androgen-independent. PC3-PIP cells were engineered to overexpress PSMA, whereas PC3-FLU cells were transduced with an empty vector and therefore do not express the receptor [28]. This matched pair of cell lines allows a clear comparison between PSMA-specific and non-specific binding under identical experimental conditions.
The cellular uptake and internalization of [^{111}In]In–IPBA–PSMA–PEG–DOTA were evaluated in PSMA-positive (PC3-PIP) and PSMA-negative (PC3-FLU) prostate cancer cells to confirm PSMA-specific binding. The total, membrane-bound, and internalized fractions were quantified using a gamma-counter, as described in the Materials and Methods section. The total uptake was calculated as the sum of the surface-bound and internalized fractions and expressed as a percentage of the total added activity per well (n = 4, mean ± SD).
In the following figure 3.34 the chemical structures of [^{111}In]In–IPBA–PEG–DOTA–PSMA and [^{111}In]In–PSMA-617 are presented. The structure of PSMA-617 was taken from the study reported by Santos et al. [51].

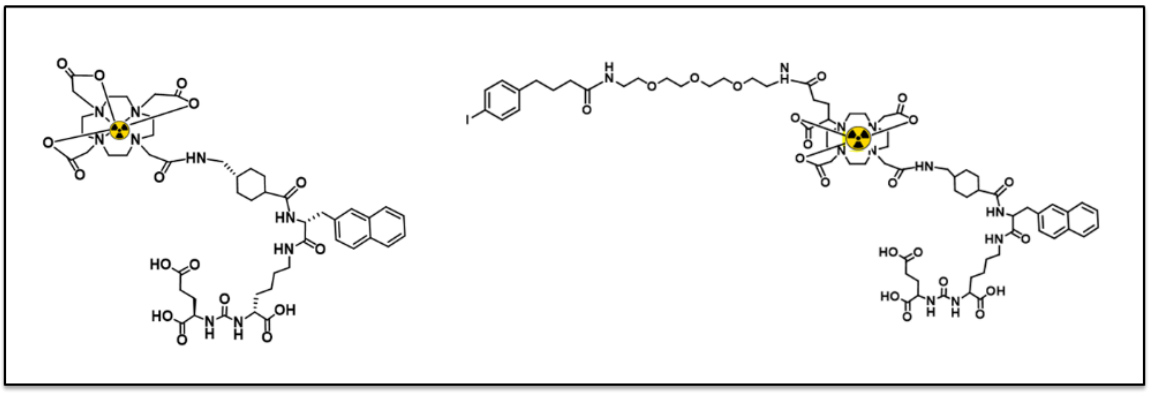

Figure 3.34: Chemical structures of [^{111}In]In–PSMA-617 (left) and [^{111}In]In–IPBA–PEG–DOTA–PSMA (right) used in the cellular uptake and internalization studies. The structure of [^{111}In]In–PSMA-617 was adapted from Santos et al. [51].

PC3-PIP

Figure 3.35 shows the cellular uptake and internalization of [^{111}In]In–IPBA–PEG–DOTA–PSMA compared with [^{111}In]In–PSMA-617 in PSMA-positive PC3-PIP cells. The data for [^{111}In]In–PSMA-617, where the tracer was evaluated under similar experimental conditions.

Both tracers display a clear time-dependent increase in total uptake, indicating active PSMA-mediated binding and internalization. However, [^{111}In]In–PSMA-617 reaches much higher uptake values, close to 70% of the total applied activity after 4 hours, whereas [^{111}In]In–IPBA–PEG–DOTA–PSMA reaches around 25–30%.

This difference should not be directly interpreted as a lower targeting efficiency of the new compound, since the two assays were performed using radiocomplexes with different specific activities. The specific activity indicates the amount of radioactivity per quantity of compound and strongly influences receptor-mediated binding. A higher specific activity means that fewer non-radioactive molecules are present, reducing competition for receptor binding and leading to apparently higher uptake values. Conversely, a lower specific activity increases the proportion of unlabeled molecules, which can occupy binding sites without contributing to the radioactive signal, resulting in lower measured uptake [56]. Therefore, the higher specific activity used for [^{111}In]In–PSMA-617 reduces the amount of non-radioactive molecules competing for receptor binding, explaining the apparently higher uptake values observed when compared to [^{111}In]In–DOTA–IPBA–PEG–PSMA.

Despite this difference, [^{111}In]In–DOTA–IPBA–PEG–PSMA shows the same general trend as [^{111}In]In–PSMA-617, with both surface-bound and internalized fractions progressively increasing over time. This indicates that the new compound retains PSMA-specific binding and follows a comparable internalization mechanism. Both tracers reach a plateau after approximately 4 h, suggesting that they exhibit similar uptake and internalization kinetics.

The lower overall accumulation observed for [^{111}In]In–IPBA–PEG–DOTA–PSMA may be attributed to the labeling conditions and the presence of the PEG linker, which could introduce slight steric effects reducing receptor interaction efficiency in vitro.

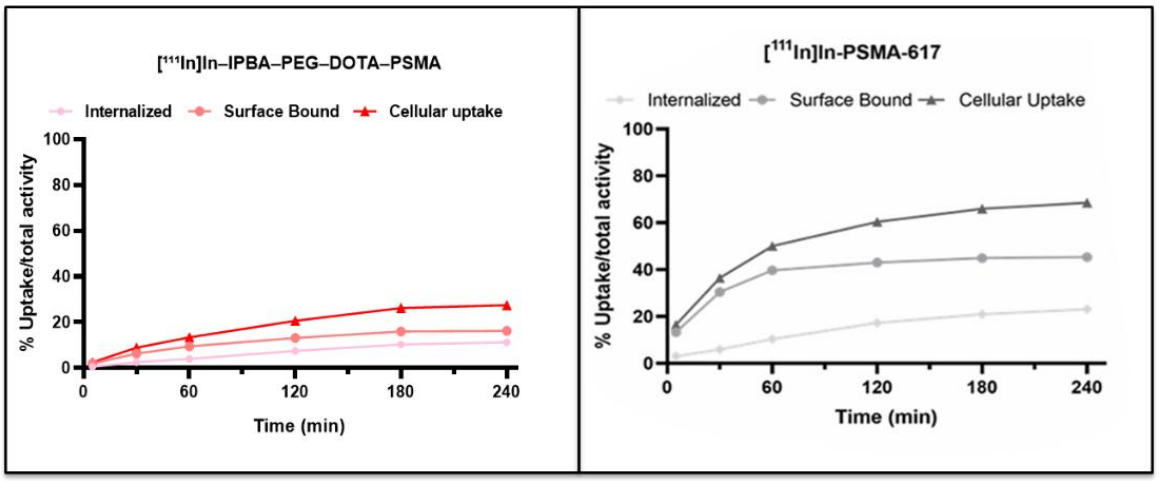

Figure 3.35: Cellular uptake and internalization of [^{111}In]In–DOTA–IPBA–PEG–PSMA (left) and [^{111}In]In–PSMA-617 (right) in PSMA-positive PC3-PIP cells. Data for [^{111}In]In–PSMA-617 were taken from Santos et al. [51].

PC3-FLU

In PSMA-negative PC3-FLU cells, the uptake of the radiocomplex remained very low at all time points (figure 3.36). Both the surface bound and internalized fractions shows minimal variation over time and together accounted for less than 1% of the total added activity. A slight increase around 60 minutes was observed, but this is likely due to weak non-specific interactions rather than specific receptor binding. As expected, no significant accumulation was detected in PSMA-negative cells, confirming that the interaction of [^{111}In]In–IPBA–PEG–DOTA–PSMA is dependent on PSMA expression. These findings indicate a high selectivity of the radiocomplex and suggest the absence of relevant non-specific binding to the cell membrane.

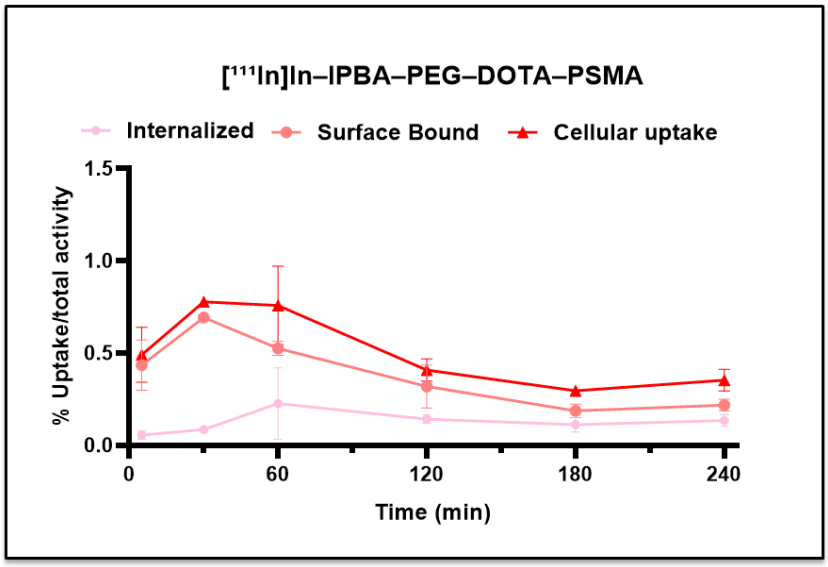

Figure 3.36: Cellular uptake and internalization of [^{111}In]In–DOTA–IPBA–PEG–PSMA in PSMA-negative PC3-FLU cells showing minimal, non-specific binding.

Blocking study

A blocking assay was performed to confirm the PSMA-specificity of the cellular uptake. In this experiment, an excess of 2-(phosphonomethyl)pentanedioic acid (2-PMPA), a potent PSMA inhibitor, was added to compete with the radiolabeled compounds for the same binding sites on the receptor. If the uptake is truly PSMA-mediated, the presence of 2-PMPA should prevent or strongly reduce tracer binding to the cells.

Figure 3.37 shows the comparison between [^{111}In]In–IPBA–PEG–DOTA–PSMA and [^{111}In]In–PSMA-617 in PSMA-positive PC3-PIP cells, with and without the PSMA inhibitor 2-PMPA.

For [^{111}In]In–IPBA–PEG–DOTA–PSMA, both the surface-bound and internalized fractions increased over time, reaching a maximum total uptake of about 16.7% after 180 minutes. When 2-PMPA was added, the cellular uptake decreased by more than 90%, confirming that the binding is predominantly PSMA-mediated.

A similar inhibition of around 90% was also observed for [^{111}In]In–PSMA-617, indicating that both tracers follow a comparable PSMA-specific mechanism of internalization and that their accumulation is almost completely blocked in the presence of the inhibitor.

Although [^{111}In]In–IPBA–PEG–DOTA–PSMA shows a lower overall accumulation (≈16.7%) compared with [^{111}In]In–PSMA-617 (≈50% after 180 min), this difference is likely due to the distinct specific activities used during radiolabeling and to the presence of the PEG linker and IPBA group, which can increase hydrophilicity and introduce mild steric hindrance. Nevertheless, the strong inhibition observed under blocking conditions clearly demonstrates that the new tracer retains high PSMA selectivity and specific binding behavior.

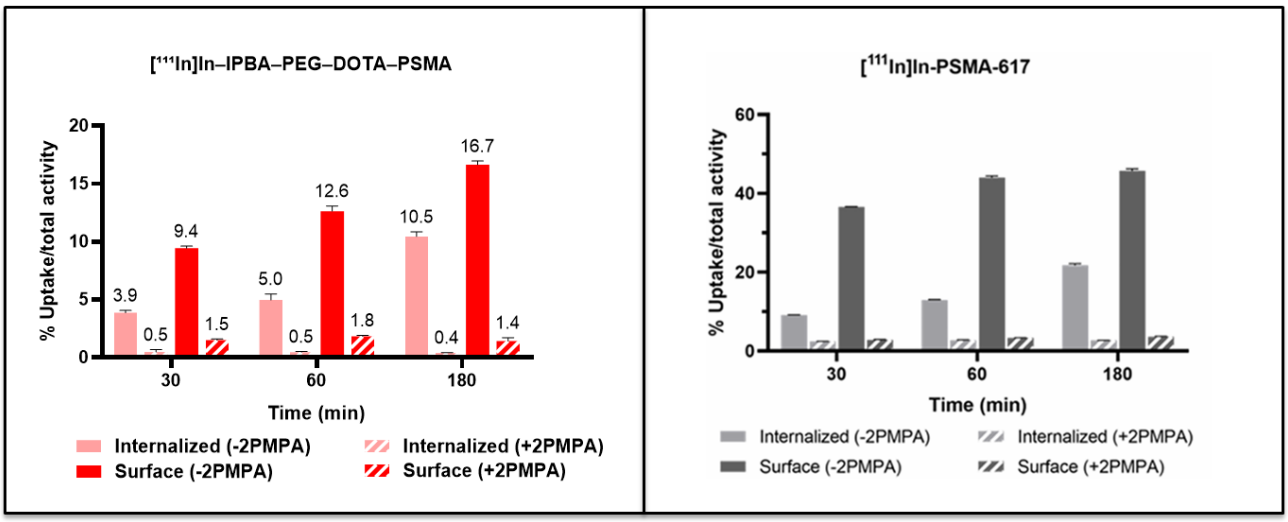

Figure 3.37: Blocking assay in PSMA-positive PC3-PIP cells showing cellular uptake and internalization of [^{111}In]In–IPBA–PEG–DOTA–PSMA (left) and [^{111}In]In–PSMA-617 (right), with and without 2-PMPA.

3.5 In Vivo Evaluation studies

In vivo studies are important to understand how the radiocomplex behaves inside a living organism.
They make it possible to evaluate its stability in biological fluids, the pharmacokinetic profile, that is how it distributes among organs, and how it is metabolized and eliminated from the body. These experiments provide essential information that cannot be obtained from in vitro tests alone, since they reflect the combined effects of metabolism, blood circulation, and tissue interaction under real physiological conditions.

3.5.1 In vivo stability

The stability of [^{111}In]In–IPBA–PEG–DOTA–PSMA was evaluated in blood at 1, 2, 4, and 24 hours after injection using radio-HPLC (figure 3.38).
At all time points, a single main peak is observed, corresponding to the intact compound, with no clear signs of degradation or transchelation.
The retention time remains stable and identical to that of the reference, showing that the complex stays chemically intact in the bloodstream for up to 24 hours.
In addition, analysis of urine samples collected at 2 and 4 hours post-injection shows the presence of the intact radioconjugate, confirming its stability.
These results confirms that the coordination between Indium and DOTA is highly stable under physiological conditions.

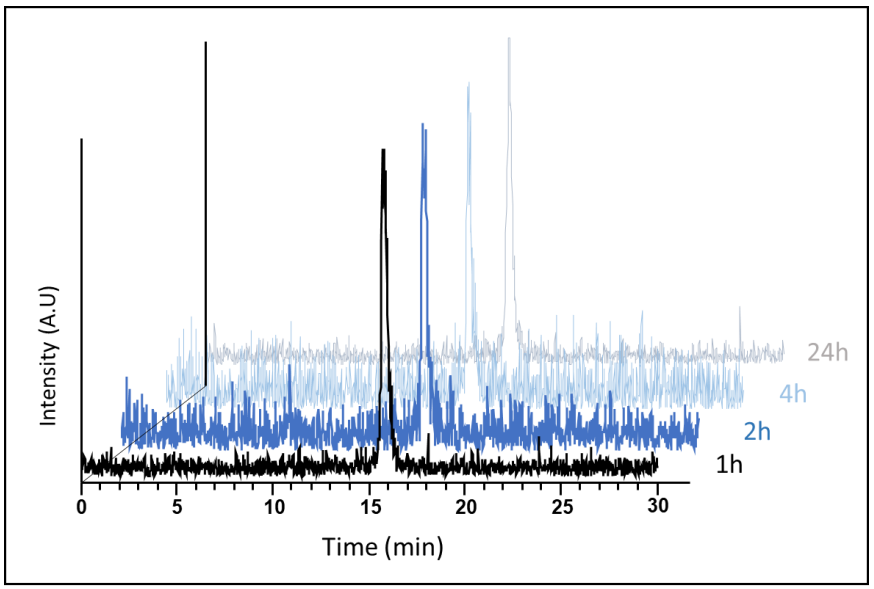

Figure 3.38: Radio-HPLC chromatograms of [^{111}In]In–IPBA–PEG–DOTA–PSMA in mouse blood at 1, 2, 4, and 24 h post-injection showing a single peak corresponding to the intact compound, confirming excellent in vivo stability.

3.5.2 Biodistribution

Biodistribution studies are used to see how a radiotracer spreads in the body after it is injected. They show how much of the compound stays in the blood, how it moves into different organs, and how it is cleared over time. By measuring the percentage of injected activity per gram of tissue (%IA/g), it is possible to evaluate blood retention and organ uptake, giving useful information about how albumin binding affects the tracer's behavior in vivo.

As shown in figure 3.39, [^{111}In]In-IPBA-PEG-DOTA-PSMA shows the highest uptake in the blood at early time points (around 23% ID/g at 1 h), which then slowly decreaseas to about 10% ID/g at 24 h. This gradual decline indicates a slow blood clearance and prolonged circulation time, in line with the expected albumin binding of the compound.

High uptake is also seen in the kidneys, suggesting that part of the tracer is eliminated through the renal route. Moderate uptake is also observed in the liver, suggesting that part of the compound is cleared through the hepatobiliary system. Slight activity in the lungs probably reflects residual blood activity or nonspecific distribution rather than active uptake.

In contrast, uptake in the intestine, heart, and brain is very low, showing limited nonspecific accumulation. The very low brain uptake confirms that the tracer does not cross the blood–brain barrier.

These data indicate that [^{111}In]In-IPBA-PEG-DOTA-PSMA remains in circulation for a long time and is cleared through both renal and hepatobiliary pathways, which is consistent with its moderate lipophilicity and ability to bind albumin.

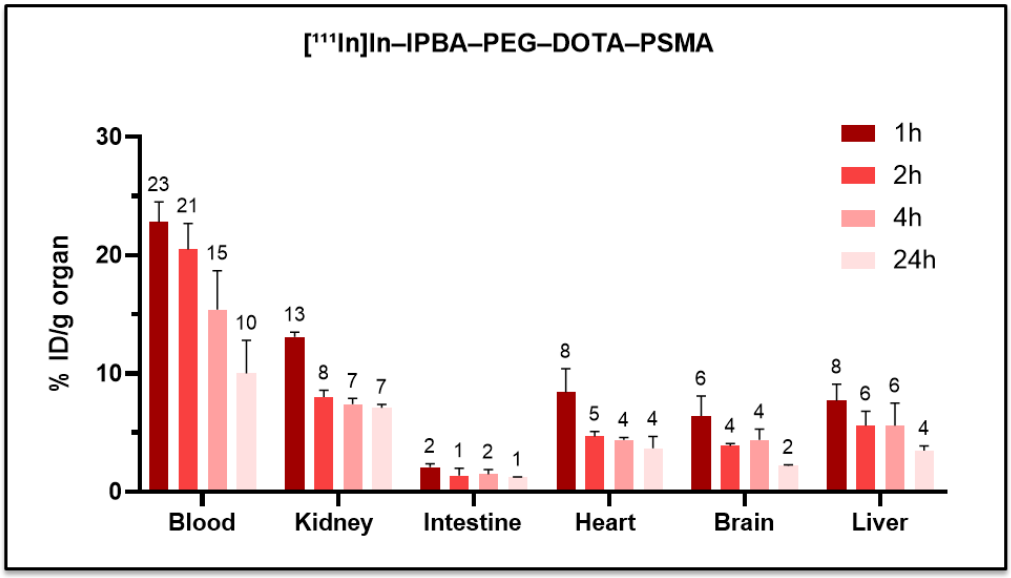

Figure 3.39: Biodistribution of [^{111}In]In–IPBA–PEG–DOTA–PSMA in major organs (blood, kidney, intestine, heart, brain) at 1, 2, 4, and 24 h post-injection.

A comparison between the biodistribution profile of the heterobivalent compound and [^{111}In]In–PSMA-617 was performed to evaluate the effect of the IPBA–PEG modification on the pharmacokinetic behavior.
Figure 3.40 represents the blood activity over time for both tracers. As shown in the graph, [^{111}In]In–IPBA–PEG–DOTA–PSMA exhibits a much slower clearance than [^{111}In]In-PSMA-617. The albumin-binding compound remains in circulation for a longer time, whereas PSMA-617 is rapidly cleared, with most of the injected activity excreted within the first hours post-injection.
The IPBA-PEG modification increases lipophilicity and promotes reversible binding to serum albumin, reducing the glomerular filtration rate and leading to a slower elimination from the bloodstream.

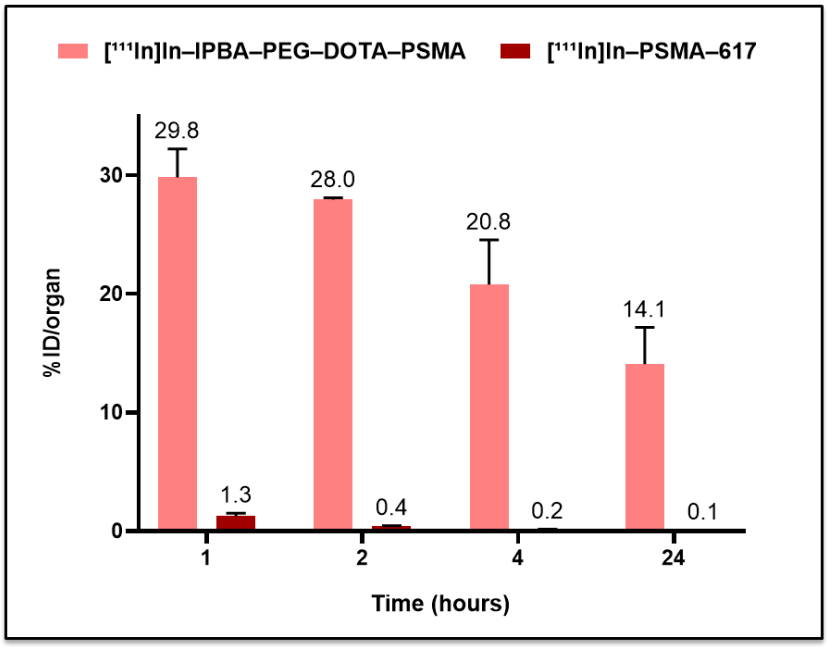

Figure 3.40: Comparison of blood retention for [^{111}In]In–IPBA–PEG–DOTA–PSMA and [^{111}In]In–PSMA-617 over time.

As seen in figure 3.41, [^{111}In]In–PSMA-617 shows higher kidney uptake at early time points compared to [^{111}In]In–IPBA–PEG–DOTA–PSMA. At 1 hour, the uptake of [^{111}In]In–PSMA-617 reaches about 8 %ID/organ, while [^{111}In]In–DOTA–IPBA–PEG–PSMA shows a lower value of 4.96 %ID/organ. This indicates that PSMA-617, which does not bind to albumin, is more available for renal filtration and therefore cleared faster from the bloodstream.
Over time, both tracers show a clear decrease in kidney activity. For [^{111}In]In–PSMA-617, the uptake drops by almost 98% from 8.06 %IA/g at 1 hour to 0.14 %IA/g at 24 hours, confirming its rapid elimination through the kidneys. In contrast, [^{111}In]In–IPBA–PEG–DOTA–PSMA decreases more slowly, by about 47% from 4.96 to 2.63 %ID/organ, showing a higher retention consistent with albumin binding domain.
This behavior suggests that a significant fraction of [^{111}In]In–DOTA–IPBA–PEG–PSMA remains bound to albumin in circulation, making it less accessible for immediate filtration but allowing for a slower clearance.
However, these results confirm that albumin binding extends blood retention and delays renal elimination compared to [^{111}In]In–PSMA-617.

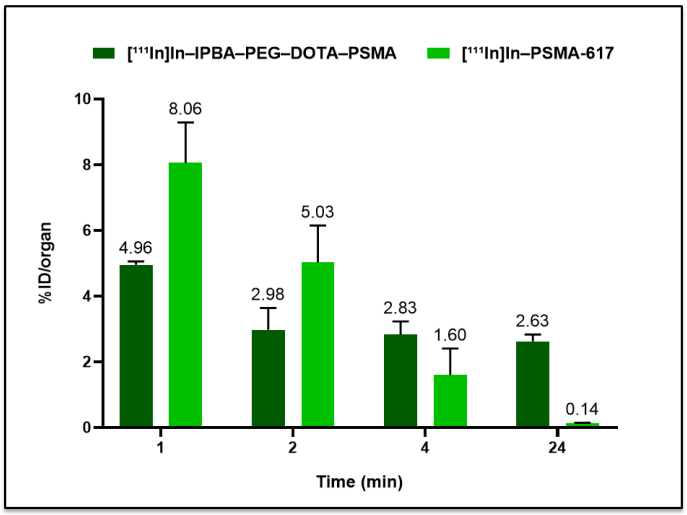

Figure 3.41: Kidney uptake of [^{111}In]In–IPBA–PEG–DOTA–PSMA and [^{111}In]In–PSMA-617 at 1, 2, 4, and 24 h post-injection showing slower renal clearance for the albumin-binding compound.

In summary, the IPBA-PEG modification effectively prolongs blood residence, reduces early renal excretion, and limits nonspecific tissue uptake. These pharmacokinetic features confirm the intended role of albumin binding in improving circulation time and potentially enhancing tumor targeting.

3.6 µSPECT/CT imaging studies

SPECT/CT imaging was employed to visualize the in vivo distribution of the radiotracers and to complement the quantitative biodistribution data. This hybrid technique combines Single Photon Emission Computed Tomography (SPECT), which detects the γ-photons emitted by the radionuclide Indium-111, with Computed Tomography (CT), providing high-resolution anatomical reference.

The combination of these two modalities enables a three-dimensional reconstruction of tracer uptake within the whole animal, allowing accurate localization of radioactivity in specific organs. SPECT provides functional information about tracer kinetics and clearance, while CT defines the anatomical structures for precise coregistration.

Representative sagittal and coronal SPECT/CT images acquired 1 h after injection are shown in figure 3.42. For [^{111}In]In–IPBA–PEG–DOTA–PSMA, the signal is mainly concentrated in the thoracic region, corresponding to the heart and major vessels, indicating that a large fraction of the tracer remains in circulation. Moderate uptake is also visible in the liver and kidneys, suggesting that both renal and hepatobiliary routes contribute to its clearance. The residual activity observed in the abdominal region and the relatively low signal in the bladder confirm that elimination is still ongoing at this early time point.

In contrast, [^{111}In]In-PSMA-617 displays a different distribution profile. The vascular signal is much weaker, while intense activity is clearly detected in the kidneys and urinary bladder, consistent with rapid renal filtration and excretion. Only minimal signal remains in other organs, confirming its faster clearance and lack of albumin binding.

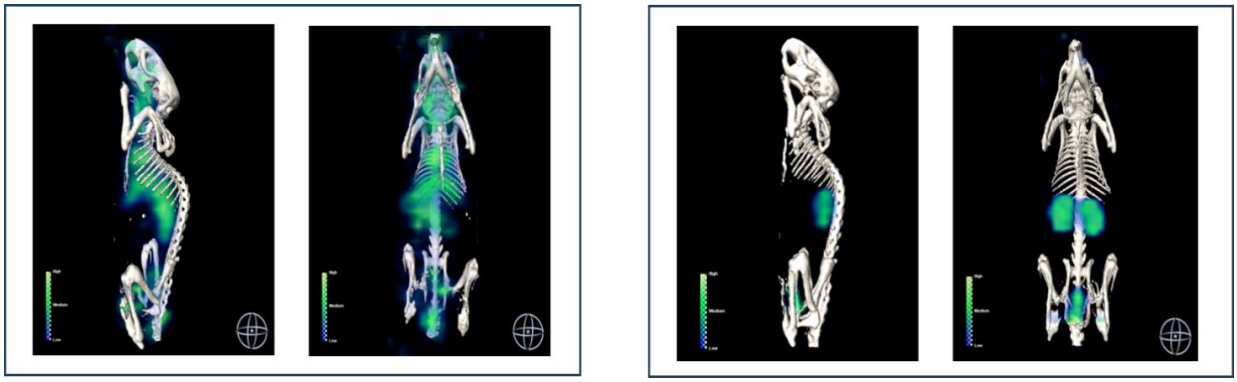

Figure 3.42: Representative SPECT/CT images acquired 1 h post-injection of [^{111}In]In–IPBA–PEG–DOTA–PSMA (left) and [^{111}In]In-PSMA-617 (right) in healthy mice.

Overall, these images visually confirm the biodistribution trends: the albumin-binding derivative [^{111}In]In–IPBA–PEG–DOTA–PSMA stays longer in circulation and is eliminated more slowly, whereas [^{111}In]In-PSMA-617 is rapidly excreted through the kidneys within the first hour after administration.

Chapter 4

Conclusions and Future Perspectives

In this thesis, the design, synthesis, and biological evaluation of a new heterobivalent radioconjugate, IPBA–PEG–DOTA–PSMA, were described. The compound was designed to combine the PSMA-targeting ability with an albumin-binding domain to improve its pharmacokinetic properties and tumor uptake. The synthesis was carried out using a DOTA prochelator with orthogonally protected arms, which made it possible to introduce the IPBA group and the PSMA-binding unit separately. This approach aimes to combine receptor specificity with reversible serum protein binding in a single molecule.

The conjugate was successfully synthesized and characterized, and it was efficiently radiolabeled with Indium-111, reaching a radiochemical purity above 95%. The resulting complex showed very good stability, both in solution and under physiological conditions. Importantly, the addition of the albumin-binding unit did not interfere with the metal chelation process or with the PSMA targeting ability.

Protein-binding experiments confirmed that the IPBA–PEG–DOTA–PSMA complex interacts with serum proteins as expected, showing a higher binding, compared to [^{111}In]In–PSMA–617. This indicates that the presence of the IPBA group helps to extend the circulation time of the radioconjugate, which could lead to higher tumor accumulation.

In vitro studies with PSMA-positive (PC3-PIP) and PSMA-negative (FLU) prostate cancer cell lines showed receptor-mediated uptake, confirming the specificity of the compound. Blocking experiments with 2-PMPA further demonstrated that the uptake is PSMA dependent.

In vivo biodistribution and μSPECT/CT imaging studies revealed slower blood clearance and lower kidney uptake for [^{111}In]In–IPBA–PEG–DOTA–PSMA compared to [^{111}In]In–PSMA–617, supporting the positive effect of the albumin-binding domain on the overall pharmacokinetic profile.

Altogether, these results demonstrate the successful development of a new albumin-binding PSMA radioconjugate with improved biological behavior. The introduction of the IPBA moiety helped to increase blood retention without reducing PSMA affinity, showing a promising balance between stability, selectivity, and circulation time.

Future work should focus on extending this design to therapeutic radionuclides such as ^{177}Lu, a β^- emitter commonly used in targeted radiotherapy, to study its therapeutic potential. Additional in vivo experiments in prostate cancer xenograft mouse models will also be important to evaluate tumor uptake, retention, and therapeutic response under more realistic biological conditions. These studies, together with pharmacokinetic and dosimetric evaluations, will be

essential to confirm the potential of this new albumin-binding PSMA radioconjugate for future clinical translation in prostate cancer theranostics.

Bibliography

[1] M. Bilal et al. An overview of prostate cancer (PCa) diagnosis: Potential role of miRNAs. *Neoplasia*, 11(1):1–10, 2022.

[2] R. J. Rebello et al. Prostate cancer. *Nature Reviews Disease Primers*, 7(1):9, 2021.

[3] J. R. Packer and et al. The molecular and cellular origin of human prostate cancer. *Biochimica et Biophysica Acta*, 1863(6):1238–1260, 2016.

[4] U. Testa et al. Cellular and molecular mechanisms underlying prostate cancer development: therapeutic implications. *Medicines*, 6(3):82, 2019.

[5] J. Gandhi et al. The molecular biology of prostate cancer: current understanding and clinical implications. *Cancer Metastasis Review,* 37(2–3):367–385, 2018.

[6] W. G. Nelson, et al. Prostate cancer. Abeloff's *Clinical Oncology*, 6(1), 2020.

[7] M. Czerwińska et al. Targeted radionuclide therapy of prostate cancer: from basic research to clinical perspectives. *Molecules*, 25(7), 2020.

[8] National Cancer Institute, Hormone Therapy for Prostate Cancer, https://www.cancer.gov/types/prostate/prostate-hormone-therapy-fact-sheet.

[9] E. B. Podgorsak Radiation physics for medical physicists. second edition, Springer, Berlin–Heidelberg, 2010.

[10] R. Kadariya, Radioactive Decay: Types, Processes & Applications, https://scienceinfo.com/radioactive-decay.

[11] A. Boschi, Corso di Radioprotezione, https://www.unife.it/medicina/infermieristica/studiare/minisiti/infermieristica-clinica-nella-criticita-vitale/radioprotezione/radioprotezione_parte-i_aa-15_16.pdf.

[12] Difference Between Ionizing and Non-Ionizing Radiation, https://sciencenotes.org/difference-between-ionizing-and-non-ionizing-radiation/.

[13] Radioactive Decay, https://www.sciencefacts.net/radioactive-decay.html/.

[14] Radioactive decay - AQA, https://www.bbc.co.uk/bitesize/guides/z3tb8mn/revision/3.

[15] W. D. Loveland, et al. *Modern Nuclear Chemistry*, second edition, 2017.

[16] Open MedScience, Unlocking the Secrets of Electron Capture: A Journey Through Nuclear Transformations, https://openmedscience.com/unlocking-the-secrets-of-electron-capture-a-journey-through-nuclear-transformations/.

[17] A. Ku, et al. Auger electrons for cancer therapy – a review. *EJNMMI Radiopharmacy and Chemistry*, 4(1):27, 2019.

[18] A. Van Der Kogel and M. Joiner, Basic Clinical Radiobiology, fourth edition, London, UK: Hodder Arnold, 2009

[19] Z. Nikitaki et al. Key biological mechanisms involved in high-LET radiation therapies with a focus on DNA damage and repair. *Experimental Results,* 3(1), 2022.

[20] J. S. Lewis, Albert D. Windhorst, and Brian M. Zeglis, Eds., *Radiopharmaceutical Chemistry*. Cham, Switzerland: Springer Nature Switzerland AG, 2019.

[21] A. Dash et al. Targeted radionuclide therapy - an overview. Current Radiopharmaceuticals, 6(3):152–180, 2014.

[22] M. Boyd et al. Radiation-induced biologic bystander effect elicited in vitro by targeted radiopharmaceuticals labeled with α-, β-, and Auger electron-emitting radionuclides. *Journal of Nuclear Medicine*, 47(6):1007–1015, 2006.

[23] S. Saini and P. Gurung, A comprehensive review of sensors of radiation-induced damage, radiation-induced proximal events, and cell death. *Immunological Reviews*, 322(1):54–83, 2025.

[24] R. Baskar et al. Cancer and radiation therapy: Current advances and future directions. *International Journal of Medical Sciences*, 9(3):193–199, 2012.

[25] National Cancer Institute, External Beam Radiation Therapy (EBRT), https://www.cancer.gov/about-cancer/treatment/types/radiation-therapy/external-beam

[26] Orchid Cancer Research, Radiotherapy for Localised Prostate Cancer. https://orchid-cancer.org.uk/prostate-cancer/localised-radiotherapy/

[27] C. Chargari et al. Brachytherapy: An overview for clinicians. *A Cancer Journal for Clinicians*, 69(5):386–401, 2019.

[28] F. B. Payolla et al. Radiopharmaceuticals for diagnosis in nuclear medicine: a short review. *Ecletica Quimica*, 44(3):11–19, 2019.

[29] D. Volterrani et al. *Fondamenti di medicina nucleare. Tecniche e applicazioni*. Springer-Verlag, 2010.

[30] J. S. Lewis et al. *Radiopharmaceutical Chemistry.* Cham, Switzerland: Springer Nature Switzerland AG, 2019.

[31] J. Malcolm et al. Targeted radionuclide therapy: new advances for improvement of patient management and response. *Cancers,* 11(2):268, 2019.

[32] A. I. Kassis Therapeutic radionuclides: biophysical and radiobiologic principles. *Seminars in Nuclear Medicine*, 38(5):358–366, 2008.

[33] S. Tronchin et al. Dosimetry in targeted alpha therapy. A systematic review: Current findings and what is needed. *Physics in Medicine and Biology*, 67(9), 2022.

[34] J. A. O'donoghue and T. E. Wheldon, Targeted radiotherapy using Auger electron emitters. *Physics in Medicine and Biology*, 41(10):1973–1992, 1996.

[35] A. Ku et al. Auger electrons for cancer therapy – a review. EJNMMI *Radiopharmacy and Chemistry*, 4(1):27, 2019.

[36] J. P. Pouget et al. Clinical radioimmunotherapy-the role of radiobiology. *Nature Reviews Clinical Oncology*, 8(12):720–734, 2011.

[37] F. L. Thorp-Greenwood and M. P. Coogan, Multimodal radio- (PET/SPECT) and fluorescence imaging agents based on metallo-radioisotopes: Current applications and prospects for development of new agents. *Dalton Transactions*, 40(23):6129–6143, 2011.

[38] University of Toronto, Environmental Health & Safety. Nuclide In-111 Decay. https://ehs.utoronto.ca/our-services/radiation-safety/nuclide-in-111decay/.

[39] E. A. M. Ruigrok et al. The future of PSMA-targeted radionuclide therapy: An overview of recent preclinical research*, Pharmaceutics*, 11(11):560, 2019.

[40] D. Abou et al. Prostate cancer theranostics – an overview. *Frontiers in Oncology*, 10:884, 2020

[41] L. Emmett, Changing the Goal Posts: Prostate-specific Membrane Antigen Targeted Theranostics in Prostate Cancer. *Seminars in Oncology Nursing*, 36(4), 2020.

[42] K. A. Plichta et al. Prostate-specific membrane antigen (Psma) theranostics for treatment of oligometastatic prostate cancer. *International Journal of Molecular Sciences*, 22(22), 2021.

[43] M. C. Sobral et al. Two Targets, One Mission: Heterobivalent Metal-Based Radiopharmaceuticals for Prostate Cancer Imaging and Therapy. *ChemMedChem*, 20(11), 2025.

[44] M. Brandt et al. Mini-review: Targeted radiopharmaceuticals incorporating reversible, low molecular weight albumin binders. *Nuclear Medicine and Biology,* 70:46–52, 2019.

[45] C. Müller et al. DOTA conjugate with an albumin-binding entity enables the first folic acid-targeted 177Lu-radionuclide tumor therapy in mice. *Journal of Nuclear Medicine*, 54(1):124–131, 2013.

[46] C. A. Umbricht et al. Preclinical Development of Novel PSMA-Targeting Radioligands: Modulation of Albumin-Binding Properties to Improve Prostate Cancer Therapy. *Molecular Pharmaceutics*, 15(6):2297–2306, 2018.

[47] C. V. Cruz Saucedo et al. Desarrollo de un método de extracción en fase sólida (SPE) para la determinación de amikacina en plasma humano por HPLC-MS/MS. *Proceedings of the V Simposio Nacional de Ciencias Farmacéuticas y Biomedicina*, Universidad Autónoma del Estado de Morelos, Cuernavaca, Mexico, 2018.

[48] J. Torres, The Basics of Running a Chromatography Column. https://bitesizebio.com/29947/basics-column-chromatography/.

[49] Antec Scientific, Che cos'è l'HPLC?. https://antecscientific.com/it/prodotti/tecniche/che-cose-lhplc/.

[50] C. Ho et al. Electrospray Ionisation Mass Spectrometry: Principles and Clinical Applications. *Clinical Biochemist Reviews*, 24(1):3–12, 2003.

[51] J. F. Santos et al. Synthesis and Preclinical Evaluation of PSMA-Targeted 111In-Radioconjugates Containing a Mitochondria-Tropic Triphenylphosphonium Carrier. *Molecular Pharmaceutics*, 21(1):216–233, 2024.

[52] M. C. Wenlock et al. A method for measuring the lipophilicity of compounds in mixtures of 10. *Journal of Biomolecular Screening*, 16(3):348–355, 2011.

[53] L. Xue et al. High-throughput barcoding of nanoparticles identifies cationic, degradable lipid-like materials for mRNA delivery to the lungs in female preclinical models. *Nature Communications*, 15(1), 2024.

[54] S. Boinapally et al. Preclinical Evaluation of a New Series of Albumin-Binding 177Lu-Labeled PSMA-Based Low-Molecular-Weight Radiotherapeutics, *Molecules*, 28(16), 2023.

[55] E. Rutkowska et al. Lipophilicity – methods of determination and its role in medicinal chemistry. *Acta Poloniae Pharmaceutica – Drug Research*, 70(1):3–18, 2013.

[56] G. Luurtsema et al. EANM guideline for harmonisation on molar activity or specific activity of radiopharmaceuticals: impact on safety and imaging quality. *EJNMMI Radiopharmacy and Chemistry*, 6(1):31,2021